BEUTH UNIVERSITY OF APPLIED SCIENCES BERLIN

Characterization and frequency stabilization of a continuous dye laser system for molecular spectroscopy

by

Johannes Seifert

A thesis submitted in partial fulfillment for the
degree of Master of Engineering in Applied Physics - Medical Engineering

completed at the
Department of Molecular Physics
of the
Fritz Haber Institute of the Max Planck Society
in Berlin.

June 2021

Under the supervision of

Prof. Dr. Gerard Meijer
from the Department of Molecular Physics, FHI Berlin

and Prof. Dr. Ingeborg Beckers
from the Department of Medical Physics, Beuth University of Applied Sciences Berlin.

Johannes Seifert
Beuth University of Applied Sciences Berlin
M.Eng. Applied Physics - Medical Engineering
889170

Eigenständigkeitserklärung

Hiermit erkläre ich, dass ich die vorliegende Abschlussarbeit selbstständig verfasst und keine anderen als die angegebenen Quellen und Hilfsmittel benutzt habe.

Berlin, den 14.06.2021

Johannes Seifert

Abstract

This thesis reports on the characterization and frequency stabilization of a continuous wave ring dye laser and the experimental usage for molecular spectroscopy. The Coherent-899-21 ring dye laser and the new components and software are described. The beam divergence Θ were determined for the first time with the new components. The tune-ability and frequency scanning of the laser is compared with different frequency stabilization methods.

The laser beam is coupled into a pulsed dye amplifier and the laser pulses were used for spectroscopy. A factory-given stimulated Brillouin scattering frequency shift of the pulsed dye amplifier is investigated and measured with different spectroscopy methods.

The laser is used on the molecular beam machine for extended spectroscopic studies on aluminum monofluoride, to determine the line positions of the $v = 5$ transitions in aluminum monofluoride with the highest accuracy possible. Therefore a more detailed look at this diatomic molecule and especially of the $b^3\Sigma^+, v = 5//A^1\Pi, v = 6$ perturbed complex is carried out.

As final measurement, the laser beam of the ring dye laser is used for saturation spectroscopy to measure a Lamb-dip, which defines the instrumental inherent linewidth of the laser.

Abstract

Diese Thesis berichtet über die Charakterisierung und Frequenzstabilisierung eines kontinuierlichen Ringfarbstofflasers und die experimentelle Nutzung für Molekülspektroskopie. Der Ringfarbstofflaser Coherent-899-21 sowie die neuen Komponenten und die Software werden beschrieben. Die Strahldivergenz Θ wurde erstmalig mit den neuen Komponenten bestimmt. Die Durchstimmbarkeit und Frequenzabtastung des Lasers wird mit verschiedenen Frequenzstabilisierungsmethoden verglichen.

Der Laserstrahl wird in einen gepulsten Farbstoffverstärker eingekoppelt und die Laserpulse wurden für die Spektroskopie verwendet. Eine werksseitig vorgegebene stimulierte Brillouin-Streuung Frequenzverschiebung des gepulsten Farbstoffverstärkers wird untersucht und mit verschiedenen Spektroskopiemethoden gemessen.

Der Laser wird an der Molekularstrahlmaschine für erweiterte spektroskopische Untersuchungen an Aluminiummonofluorid eingesetzt, um die Linienpositionen der $v = 5$ Übergänge in Aluminiummonofluorid mit höchstmöglicher Genauigkeit zu bestimmen. Dazu wird eine genauere Betrachtung dieses zweiatomigen Moleküls und insbesondere des gestörten Komplexes $b^3\Sigma^+, v = 5//A^1\Pi, v = 6$ durchgeführt.

Als abschließende Messung wird der Laserstrahl des Ringfarbstofflasers zur Sättigungsspektroskopie verwendet, um einen Lamb-Dip zu messen, der die instrumenteneigene Linienbreite des Lasers definiert.

Contents

List of Figures

List of Tables

Chapter 1

Introduction

The study of molecular interactions with electromagnetic radiation enables a determination of the transitions in atoms and molecules. The resulting spectra can be looked at as fingerprints of atoms and molecules when plotted as a function of frequency. To characterize a molecule as accurate as possible, the measurement should be as interaction-free as possible.

The main goal of the ultracold molecule laboratory in the Molecular Physics department at the Fritz Haber Institute is to perform laser cooling of diatomic molecules. The experiments of the present work are completed there. The interaction with lasers will allow to trap and to cool the molecules to very low temperatures of a few millionths of a degree above absolute zero. The advantage of molecules at such low temperature is that they move with a speed of about 1 cm/s, compared to 300 m/s at room temperature. This results in the possibility to study the interactions between the molecules and light with unprecedented precision [14].

First spectroscopic investigations indicate that aluminum monofluoride (AlF) is a candidate for laser cooling [15]. The main cooling cycle has been identified between the ground state X and the first electronic state A, along the so-called $X \leftrightarrow A$ transition in the singlet manifold. It allows cooling up to mK temperatures. Afterwards a second cooling cycle between the X state and the metastable a state in the triplet manifold could enable cooling down to the μK regime. Therefore the interest in the triplet state has grown and the resolution of spectra should be as high as possible. Transitions between singlet and triplet manifolds are typically difficult to excite - high power lasers with a small

bandwidth are needed because the transitions are mostly forbidden. However, if two or more molecular states in the singlet and triplet manifold come close or have almost the same energy, perturbations can happen which increases the coupling between these states - a so-called doorway state between the singlet and triplet manifold can result. A goal of this thesis is to identify these pertubations in aluminum monofluoride and to characterize them precisely.

Continuous wave (cw) dye lasers are known for their small linewidth down to kHz and a high tune-ability of the frequency range. In this thesis a ring dye laser (RDL), the Coherent-899-21 and the new components and software are described. Using a laser frequency stabilization which was developed in collaboration with the FHI electronics lab allows to actively stabilize and to scan the frequency of the RDL. Furthermore, this laser has been used in an experiment for extended spectroscopic studies on AlF with the goal to determine the line positions of the transitions in AlF with the highest accuracy possible.

The outline of this thesis is that first, there will be a basic explanation of the working-principle of lasers. In the second chapter a more specific view of the Coherent-899-21 RDL is given. The RDL output laser beam is coupled into a pulsed dye amplifier (PDA) which amplifies the laser intensity at the cost of a broader bandwith of the resulting laser pulse which is not as narrow as the cw RDL anymore. In the fourth chapter, these laser-pulses are then used for spectroscopy in a supersonic molecular-beam machine. To compare the recorded spectra, there will be a more detailed look at the diatomic molecule aluminum monofluoride and especially of the perturbed states. As final measurement, the cw laser beam of the RDL is used for saturation spectroscopy to measure a Lamb-dip. This defines the instrumental inherent linewidth of the laser.

1.1 Electromagnetic Radiation

Electromagnetic radiation, waves of an electromagnetic field, cover a wide spectrum of frequency. Light interacts with matter differently according to its frequency. Ultraviolet and visible light can excite valence electrons, changing their atomic or molecular orbital.

Infrared radiation changes the molecular vibration of molecules while microwave radiation typically couples with rotations in molecules. Radio-frequency radiation interacts with the hyperfine structure in atoms or molecules.

The frequency ν is given in the unit [Hz]. Together with the speed of light, the wavelength λ is declared as $\lambda = c/\nu$. The energy unit of wavenumbers $\tilde{\nu}$ with unit $[\mathrm{cm}^{-1}]$ is often used for the optical and near UV spectral interval. It's the reciprocal of the wavelength $\tilde{\nu} = 1/\lambda$. The angular frequency can be obtained with $\omega = 2\pi\nu$.

1.2 Light Amplification by Stimulated Emission

The term laser is the abbreviation for "Light Amplification by Stimulated Emission of Radiation". Albert Einstein had already created an important prerequisite in 1917. At that time, the physicist discovered that atoms can be stimulated to emit light quanta if they first absorb a photon of the corresponding wavelength. The emitted light has an energy corresponding to Planck-Einstein relation,

$$E = \hbar \cdot \omega \tag{1.1}$$

where E is the energy, $\hbar$ the Planck constant divided by 2π, and ω the angular frequency of an electromagnetic wave [16].

A laser works as an oscillator and amplifier for monochromatic light in the range from infrared to ultraviolet. To get an overview of how the functionality of a laser works, a two-level system will be used. This is a fundamental way in quantum mechanics to describe the eigenstates of a physical system like molecules, atoms, and ions. A ground state E_0 and an excited state E_1 of an atom can be seen in Fig. 1.1.

The ratio of population densities of those states is described with the Boltzmann-distribution with the population N.

1.2.1 Spontaneous and Stimulated Emission

The electrons can make transitions between two energy levels of an atom, while an excitation goes along with an absorption of light. This excites the electron and increases

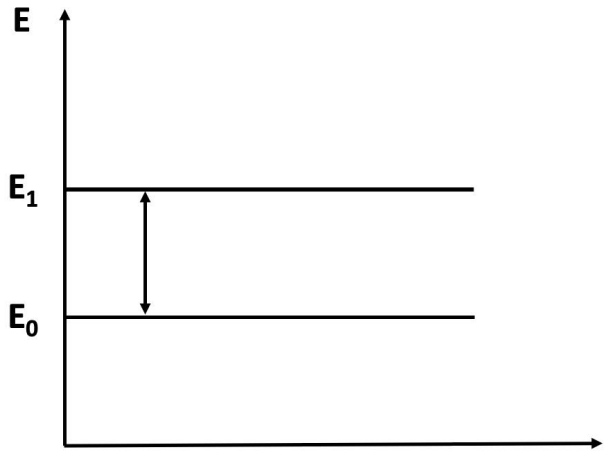

FIGURE 1.1: Energy levels of a two-level system.

the energy of the atom. In the reverse process of the de-excitation the emission of light happens together with the transition of an electron to a lower state. There are different types of energy transfer possible which can excite an electron. Energy transfer by collisions between the atoms or energy transfer by electromagnetic radiation. The energy absorption and emission are only in a narrow spectral band or so-called line. The energy difference by emission is given in the form of a photon with a characteristic frequency ν. The energy transfer by electromagnetic radiation can be split into three processes. An excited atom or molecules decays back to the ground state after a defined time, which depends on the transition probability. Then the mentioned photon is emitted with a certain frequency, which is called spontaneous emission (1). When the photons of the electromagnetic radiation hit the atoms with a resonant frequency, the atoms of the ground state E_0 are excited to the excited state E_1, which is called absorption (2). However atoms that are already in an excited state can be induced by a photon to decay to the ground state by emission of a second photon. This effect is called stimulated emission (3) and the resulting photon is in phase which amplifies the electromagnetic radiation. In thermal equilibrium, there are more atoms in E_0 than in E_1, which is why the specific schemes have to be used to obtain population inversion [17, 18].

1.2.2 Population Inversion

Only photons that are emitted can take place in an amplification, so the atoms have to be in the excited state. Unfortunately stimulated emission and absorption are proportional

to the number of available atoms and since both processes have the same proportionality constant, at best a uniform distribution can be achieved in the limiting case. With this, no light amplification can take place since the two effects become equally probable. This is why the state of population inversion is used to ensure that more atoms are in the excited state than the ground state. Population inversion is realized through optical pumping, where the electrons are excited through light absorption. Another possibility is the excitation through collisions with electrons or ions in a gas mixture. In reality one actually deals with a three- or four-level system which are used to generate population inversion. There will be a closer look at a four-level system, with the levels E_1, E_2 and E_3 as excited states. It is assumed that $E_0 < E_1 < E_2 < E_3$ and that the energy of E_1 lies between that of the other states.

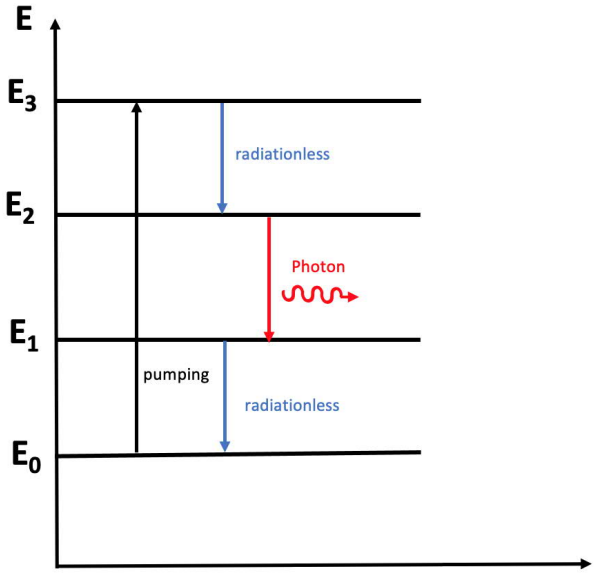

FIGURE 1.2: Energy level diagram of a four-level system.

First of all the pumping process takes part, where atoms with the frequency $\nu_{30} = (E_3 - E_0)$ will be transferred to the highest state E_3. It is necessary that these excited atoms quickly decay to E_2. This allows more transitions from $E_0 \rightarrow E_3$, because of the small population N_2. The energy released in this transition is typically either at a very different wavelength than the lasing one or it is radiationless, with the energy being transferred to vibrational motion or in a collision. These specifications must be taken into account when choosing a gas, a liquid, or a solid for lasing gain medium. If the lifetime of E_2 is longer than E_3 a population of excited state atoms will accumulate in E_2. This leads to a population inversion such that $N_3 > N_2$ and $N_3 > N_0$. This

is the prerequisite for a system such that photons of the frequency ν_{32} can be used for amplification. In reality there are four- or even more level systems because fewer atoms must be excited into upper levels and there is a wider range of frequency. Also the energy from $E_0 \rightarrow E_3$ is higher than the transition for lasing in every system. This means the frequency of the pumping light must be greater, which is realized in the laboratory with a second harmonic generation or multiple photon absorption through lower energy levels.

On the contrary, some lasers generate their output with a different mechanism. Most important the dye lasers, where the medium consists of molecule complexes. Their functionality will be describes in chapter 2.2 [18].

1.2.3 Laser Cavity

In order for a laser to actually start the lasing process it needs feedback. Similar to the electronic approach of an oscillator, the signal (the electromagnetic wave) has to be reflected into the laser medium. This is accomplished with a cavity, which exists of two mirrors around the laser medium. In this setup, a stationary field distribution only exists at certain exact resonance frequencies. These standing waves do not erase each other by interference and only such oscillation modes can establish, where the distance between the mirrors is an integer multiple of half the wavelength. Suitable wavelength λ with a constant cavity length L is defined as

$$n\lambda/2 = L, \tag{1.2}$$

with n as the number of modes [19]. Next to this frequency selection, radii of curvature and mirror distance change diffraction losses and divergence angles. The output is given by a partly transparent mirror, where care must be taken that the losses due to the decoupling are not greater than the amplification of the laser medium. A sequence of light generation can be seen in Fig. 1.3 [18].

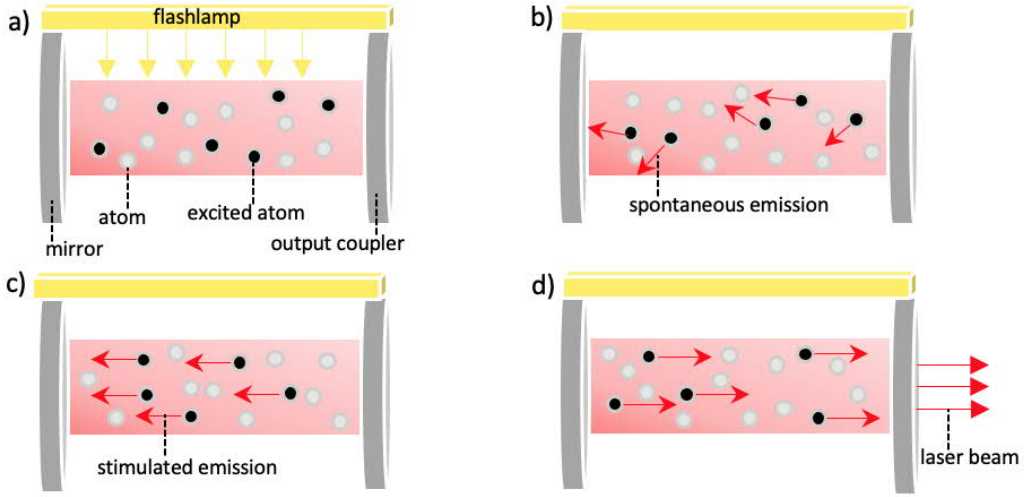

FIGURE 1.3: Schematic of a laser cavity. a) A flash-lamp excites atoms in the gain medium into an excited state which causes a population inversion. b) Spontaneous emission happens in all directions. Those happening along the cavity axis propagate though the gain medium which c) induces stimulated emission in other atoms. A standing wave establishes while the photons propagate back and forth in the cavity inducing more stimulated emission. d) The outcoupling of the light can be determined using dedicated electronics.

1.2.4 Transversal- and Longitudinalmodes

The intensity distribution in the cavity and therefore also the optical output of a laser beam can vary, because the standing waves can establish differently in the longitudinal and in the transverse direction of the cavity [20]. Depending on the alignment of the cavity mirrors the intensity distribution in the laser cavity will form a self-reproducing field distribution after several revolutions in the cavity. In principle many different distributions can establish which can mathematically be described as the eigen-solutions to the optical resonator. Very often the optimal and desired intensity distribution is that fundamental mode, the so-called called TEM_{00} mode.

Longitudinal modes are different intensity maxima as a function of the frequency. Because of 1.2 there a several emission lines. With the highest peak being the TEM_{00}, they all show a Lorentzian line profile with Gaussian peculiarities from the amplification and Doppler broadening. In practice, only one longitudinal mode is aspired, which is realized by inserting an etalon. This component has the same structure than the laser cavity and suppresses other modes without decreasing the power.

Transverse modes are a distribution of the phase position of the waves perpendicular to the direction of propagation.

1.2.5 Characteristics of Laserlight

Laser light has many different characteristics compared to 'classical' light emitted for example by the sun or a light bulb. This makes their use for interaction with matter so important. First of all laser light is monochromatic. This allows excitation of atoms and molecules at the desired resonance frequency, but the emitted frequency is depending on the emission line of the laser medium. The second property of laser light is the temporal and spatial coherence, which leads to the fact that the light is capable of interference even with large path differences. Thirdly the light has a small divergence angle, which is diffraction-limited. Only semiconductor lasers show a higher divergence angle, because of higher diffraction loss through the small cavity [21].

Due to the operating modes of a laser system, one distinguishes pulsed and continuous wave mode (cw). For continuous mode operation, pump excitation must be continuous, which also leads to constant but limited output power. For pulsed laser systems often flash lamps are used as a pump source to achieve the population inversion with the restriction that the laser pulse duration and the flash lamp pulse duration are in the same order of magnitude. But pulsed laser system can also achieve output power up to the petawatt level within ultrashort duration of femtoseconds. This is attributed to different pump excitation techniques. Next to the commonly used techniques like optical pumping and mode locking, chirped pulse amplification has to be mentioned. A special technique which was rewarded with the Nobel prize for physics in 2018 has set a new power maximum for pulsed laser [22].

A Q-Switch is a laser component, developed for modifying the loss factor of the laser cavity, so-called Q-factor. There are four major components which can be seen in Fig. 1.4. The Pockels cell consists of a birefringence crystal surrounded by two electrodes. First of all the light passes through the polarizer, transmitting only horizontally polarized light. The light passes two times through the $\lambda/4$-plate, which rotates the polarization of 90 degrees and ends up been reflected by the polarizer. With the pump energy leading to a population inversion in the medium, the loss has to be reduced to achieve lasing. When high voltage is applied to the Pockels cell, the electrodes cause an electric field in the

crystal. Because of the birefringence material, the delay of the $\lambda/4$ is compensated and the back reflection stays horizontal. This results in a minimization of the cavity loss and with all electrons decay simultaneously a laser pulse with high power (MW range) and ns duration is generated.

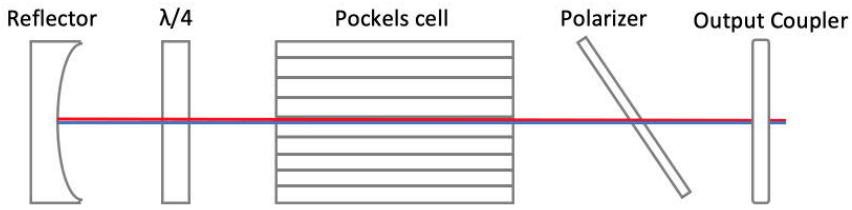

FIGURE 1.4: Components of a Q-Switch for pulsed laser systems.

An other technique mentioned to generate laser pulses is mode locking. There the axial modes, which initially oscillate independently in the cavity, are amplitude modulated with a frequency equal to the mode spacing of the laser. This ensures synchronization of the modes with a constant phase angle. They constructively interfere, producing pulses with duration down to femtoseconds [23].

Chapter 2

Characterization of a Continuous Ring Dye Lasersystem

In this chapter, the Coherent 889-21 ring dye laser (RDL) is introduced in detail. This laser is one of the main components of the experiments described in the later chapters. Lasing is achieved by pumping a laser dye (Rhodamine 6G) with a frequency doubled Nd:YAG laser which is diode-pumped, the Millennia eV 15 at 532 nm. This chapter includes both the general physical background as well as the reference to the actual application.

2.1 Laserdye as an Active Gain Medium

Dye molecules are large organic compounds soluble in solutions like ethanol, water or ethylen-glycole. The electronic energy states are divided into singlet and triplet states. In the singlet states, labeled with S, both electrons have an opposite spin and the total spin is zero. In triplet states, labeled with T, the spin of both electrons points in the same direction, equal to a total spin of $S = 1$. Triplet states are energetically below the corresponding singlet states. The states contain a wide range of vibrational and rotational excited states, which can be modeled as in an energy diagram [3].

The energy level diagram shown in Fig. 2.1, corresponds to a four-level laser. There are two pairs of singlet and triplet states each. Singlet states have a lifetime of only a few nanoseconds since the transitions are allowed. Intersystem crossing to triplet states

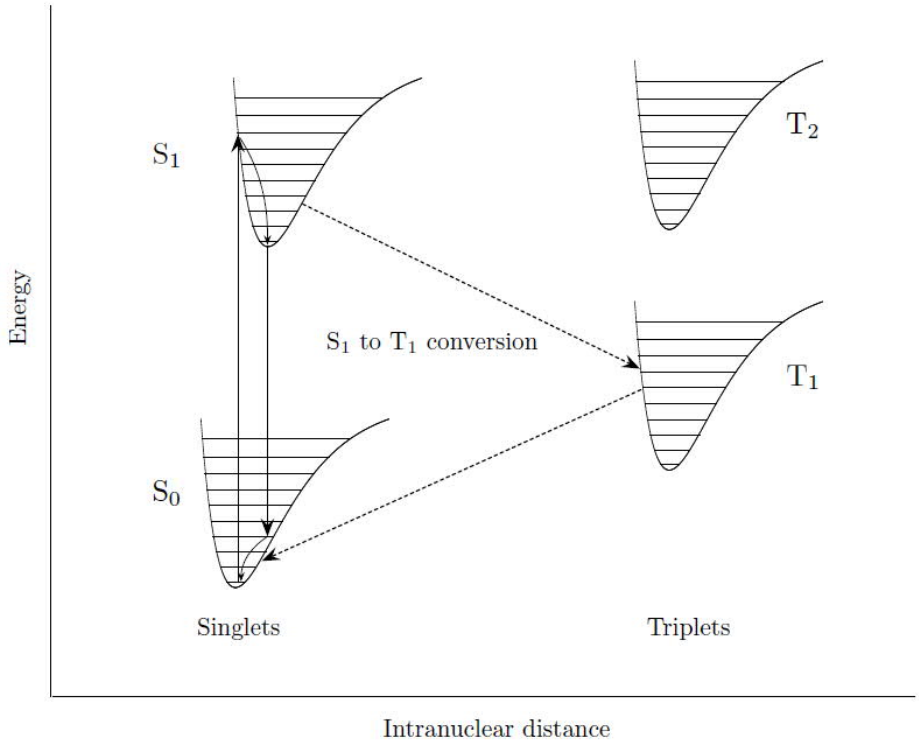

FIGURE 2.1: Electronic states of a dye laser
Figure reprinted from [1]

via spin flip is forbidden. Because of the longer lifetimes of 10^{-7}s $\rightarrow$ 10^{-3}s these states are left out of the amplification process until the decay back to singlet state. When the laser dye gets excited to a higher electronic state, the vibrational levels redistribute via inelastic collision with other molecules to the S_1, $v = 0$. This radiationless transition leads to a heating of the dye solution and a maximum population of the energy levels at the potential minimum. The optical transition for lasing will be between this level and an excited vibrational level S_0, $v \leq 1$. To determine the vibrational levels, the Franck-Condon principle is fundamental. The intranuclear distance r does not change, so the transition will be vertical and it favors a maximum S_0 to a maximum S_1. The processes take place when the dye is pumped [1, 17].

2.1.1 Absorption and Emission Levels

The bandwidth of the absorption and emission explains the high tune-ability of dye lasers. Choosing a dye such that it absorbs very well at a wavelength for which there is a powerful, fixed-wavelength pump laser available. The output efficiency determines

a dye, which can be seen in Fig. 2.2. Dyes typically cover a bandwidth of around 40-50 nm, allowing the use of the whole visible spectral range for lasing. Second-harmonic generation can be used to expand the efficient range into the UV.

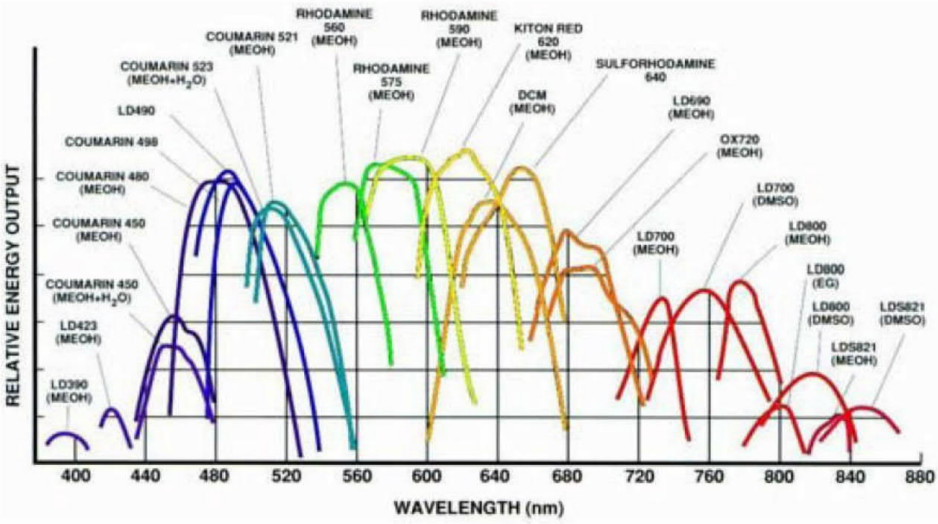

FIGURE 2.2: Spectral emission of laser dyes
Figure reprinted from [2]

Rhodamine 6G is used in the following experiments and as an example. In Fig. 2.3, the effective cross-section of the absorption and emission curves of the singlet states of Rhodamine 6G can be seen. Absorption can happen in a broad wavelength range along the $S_0 \rightarrow S_1$ transition, with a maximum by heating of the dye through a radiationless higher vibrational transition to S_1. The wide absorption curves allow to neglect a wavelength-selective pump source. The maximum absorption has a shorter wavelength corresponding to the energy level diagram $\Delta E_a > \Delta E_e$. The quantum yield by radiative transition into S_0, generates the frequency shifted emission curves. The wide curve of the stimulated emission enables a continuous tuning with a frequency selective element. Such a level scheme is the main reason to obtain population inversion in this dye laser system. The only downside is the crossing of both curves which results in absorption losses and possible power losses when switching the dye [17].

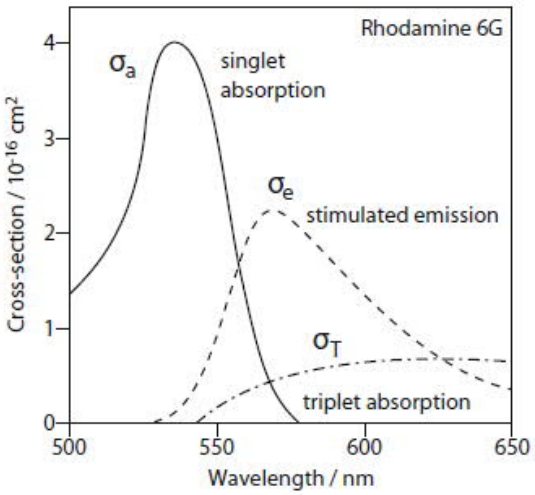

FIGURE 2.3: Rhodamine 6G absorption and emission in singlet state
Figure reprinted from [3]

2.1.2 Dye Circulator and Dye Jet

A dye jet is a method used in continuous dye laser systems to expose dye molecules in a free liquid jet to the pump laser light. The dye solution is pumped with a high backing pressure through a flat nozzle to generate a laminar flow, and a pump laser excites the molecules in this fast-flowing liquid. The dye jet streams through the focal point of the pump laser with a flow velocity of $v_s = 10$ to $100\,\mathrm{ms}^{-1}$. This results in a dwell time t_{dwell} of $1\,\mu$s which is shorter than the lifetime of the triplet state and avoids accumulating population in T_1. [17] It is important to always have new, fresh dye molecules interacting with a pump laser, that's why the molecules are circulated through a valve. Therefore the Sirah CW-2000 dye circulator is used to cool, filter, and pump the dye. A high-power motor system allows high-pressure operating of the dye jet. It consists of a 5000 ml reservoir, bypass valve, and a pressure gauge [4].

2.1.2.1 Brewster Angle

The laminar dye jet has to be under Brewster angle θ_B relative to the optical axis of the ring cavity. The Brewster angle is a specific angle where the light will transmit without reflection loss through a surface. Derived from the Fresnel equations the Brewster angle

is defined as:

$$\theta_B = \arctan(\frac{n_2}{n_1}) \tag{2.1}$$

with n as the refractive index. Under these condition of a laser beam, only that polarization direction that is under Brewster angle will start lasing. The plane liquid stream by the dye jet is also tilted under the Brewster angle to compensate for astigmatism in the folded cavity design [13].

FIGURE 2.4: The Sirah CW-2000 dye circulator.
Figure reprinted from [4]

2.1.3 Laser-Pumping with the Millennia eV 15

The Spectra Physics Millenia ev 15 is a diode-pumped, cw laser at 532 nm and is used as a pumping laser for Rhodamine 6g. The optical cavity consists of a folded cavity resonator. This type of resonator uses curved or concave mirrors to bent the optical path [24]. This results in a longer optical path, with the advantage of compact packaging. The concave mirrors induce a focal power that suppresses divergence. The laser light is produced using a diode module to pump a vanadate crystal. Vanadate absorbs the fiber-coupled output, emitting a laser beam at 1064 nm. A telescope focuses the diode pump beam through a dichroic mirror into the crystal. Afterward, a phase-matched lithium triborate crystal (LBO) frequency doubles the light to 532 nm. A temperature-regulating oven maintains the temperature of the LBO, optimizing the output power. A beam splitter and a photodiode before the output generate feedback and constant output power [25]. The threshold pump power needed depends on the pump focus and the resonator losses

of the cavity. The pump focus should be adjusted to the beam waist of the dye laser for optimum pump efficiency.

2.2 Coherent 899-21 Ring Dye Laser

The Coherent 899-21 ring dye laser (RDL) is a continuous wave laser system which can be tuned over a wide range of wavelengths. Lasing is generated by pumping an organic dye dissolved in ethylene glycol pumped with another laser or a flash lamp. To change the bandwidth of the laser, the dye can be changed to match a wanted emission spectrum as shown in Fig. 2.2.

2.2.1 Schematics of the Ring Dye Laser System

The complete ring dye laser system is shown in Fig. 2.5. The laser cavity is arranged as a ring which gives the laser its characteristic name. The mirrors $M1$ to $M4$ form the ring cavity with an exact length of $L = 1.5\,\mathrm{m}$. It prevents the laser from spatial hole burning because no standing waves are formed in it. However, a ring resonator is also more complicated to adjust [17]. The pump mirror $P1$ allows a variation of the angle through the dye jet. Optical components such as a birefringent plate, thin, and thick etalon allow single mode operation and frequency tuning. An additional reference cavity is added for frequency stabilization.

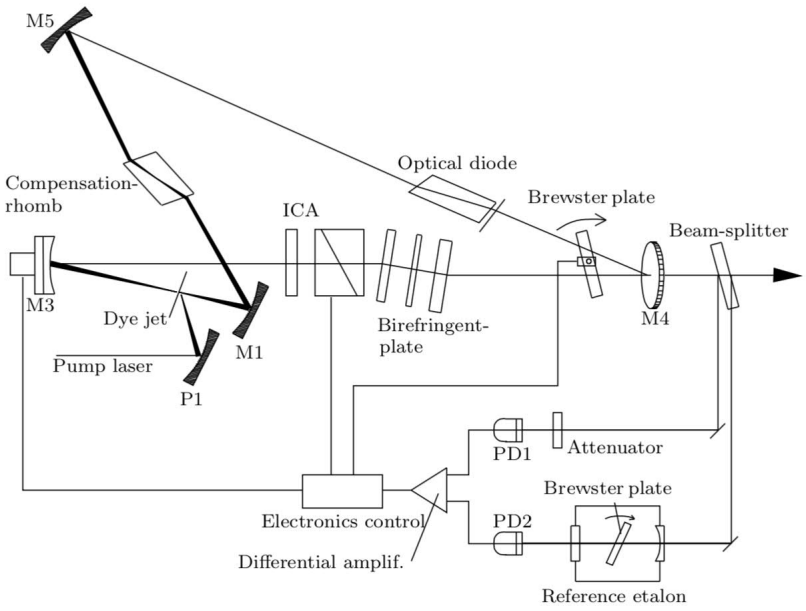

FIGURE 2.5: Overview of the RDL schematic.
Figure reprinted from [5]

2.2.2 Laser Head and Ring Cavity

The major components of the optical resonator can be seen in Fig. 2.6. To accomplish lasing an integral number of wavelengths needs to fit in the total round-trip length of the cavity. Together with the length L the longitudinal mode spacing can be calculated with:

$$L = \frac{\lambda}{2} n \tag{2.2}$$

This leads to a n at 580 nm of $\approx 5.2{\cdot}10^6$. The number of modes is one of the factors which determines the necessary pumping power to operate the laser. The lowest transverse mode, the TEM_{00} mode, has the most intensity on the beam axis. Therefore the elements of the laser are oriented that after the reflection loss, only the TEM_{00} is dominant and starts lasing.

An advantage of the ring-cavity is that one has the laser light propagating only in one direction. The combination of a fixed polarization rotation by a $\lambda/2$-plate and of a direction-dependent polarization rotation in a Faraday rotator, an optical diode, is used. The material of the diode changes the optical activity by an external magnetic

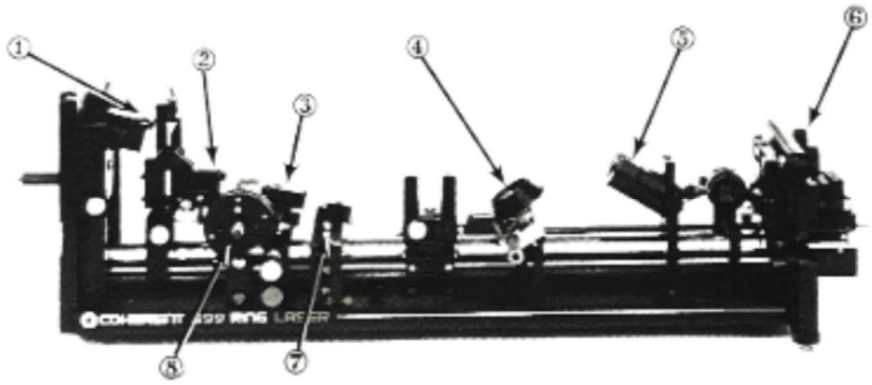

FIGURE 2.6: Laser head components. (1) Upper fold mirror M5. (2) Lower fold mirror M1. (3) Pump mirror P1. (4) Birefringent plate. (5) Optical diode. (6) Output coupler M4. (7) Intermediate fold mirror M1. (8) Dye gain jet.
Figure reprinted from [6]

field, depending on the angle between the propagation direction of the light and the magnetic field. An output analyzer, cuts of horizontally polarized light and transmits vertical (aligned to the input polarization) polarized light. The $\lambda/2$-plate is arranged in such a way that the polarization is rotated back by the same angle. When light travels forwards through the cavity, the polarization of the light undergoes two rotations, which set the light back to its incoming polarization and allows passing through the analyzer. Light traveling in the other direction will rotate over 2 times the angle. Because of all the polarization pensitive elements in the cavity, this is enough to extinguish the horizontal polarized light. The tendency to mode-hop through hydrodynamical fluctuations and the homogeneously broadening of organic dye molecules need frequency selectivity and control. Passive frequency control is achieved with a series of intracavity filters. The birefringent plate is based on the interference of polarized light that passes through birefringent crystals and can be compared to a rotation through a grid:

$$2d\cos\Theta = m\lambda \quad with \quad m = 1, 2... \tag{2.3}$$

This plate is uncoated and arranged at a Brewster angle. The operational bandwidth is narrowed for single mode operation with the insertion of the intracavity etalon assembly (ICA), which consists of a thick and thin etalon. The etalons work in the same way as a cavity. If the wavelength of the light matches the refraction index n and the thickness

of the plate d, a standing wave is generated and transmitted. Together with the angle of incidence θ, the transmission peaks are defined as:

$$\lambda_m = \frac{1}{m} 2nd\cos\theta \quad with \quad m = 1, 2... \tag{2.4}$$

The thin etalon narrows the longitudinal modes and the thick etalon narrows the spectral range above the laser threshold to single mode. The function of the single elements and their transmission curves can be seen in Fig. 2.7. The angle of incidence θ of the thin etalon is controlled with a galvanometer drive. A piezoelectric transducer varies the thickness of the thick etalon.

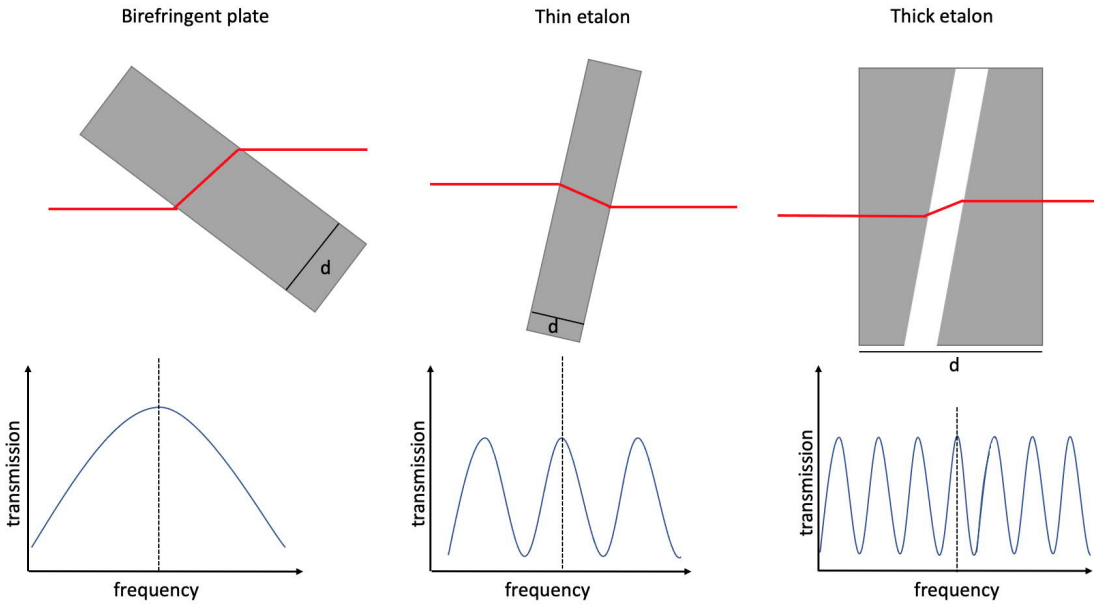

FIGURE 2.7: Intracavity elements with schematics of their transmission curves for laser mode selection.

The continuous tuning of such a single mode dye laser requires the synchronous change of the resonator length and the transmission maxima of the selecting elements [1, 6]. The three transmission curves multiplied define the single mode selection curve. This results in only one laser cavity mode which is above lasing threshold due to the losses generated by the combined transmission curve, which can be seen in Fig. 2.8.

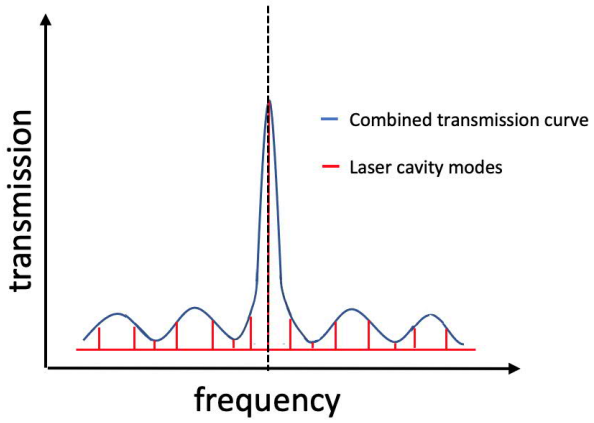

FIGURE 2.8: Schematic of the combined transmission curves from Fig. 2.7.

Laser scanning is realized by the galvanometer-driven Brewster plate in relation to the thin etalon. To scan over a large range, the working-principle of a Brewster plate, as a function of the angles and thickness are given in Fig. 2.9. The incoming beam (red) is displaced over the height h. The optical path length is $L = nd/\cos(\alpha_r)$, with n as the refractive index of the material, d the thickness of the material, and α_r the angle of refraction. Without the plate, the laser beam would travel only over the distance x. Together with α_b as Brewster angle, $x = d(\cos\alpha_b + \sin\alpha_b \tan\alpha_r)$. When the plate is tilted, the optical path length of the cavity L and the distance x change. Under the consideration of the Brewster angle $\tan\alpha_b = n$, the angle variation of the Brewster plate $d\alpha$ gives a value for a scan per frequency $d\nu$.

$$d\alpha = -\frac{L\lambda n\sqrt{1+n^2}}{cd(n^2-1)} \tag{2.5}$$

With a quartz plate of d=2 mm, n=1.54, and the laser properties L=1.5 m, λ= 580 nm: $d\alpha \approx 3 \cdot 10^{-3}$ radiant per GHz scan.

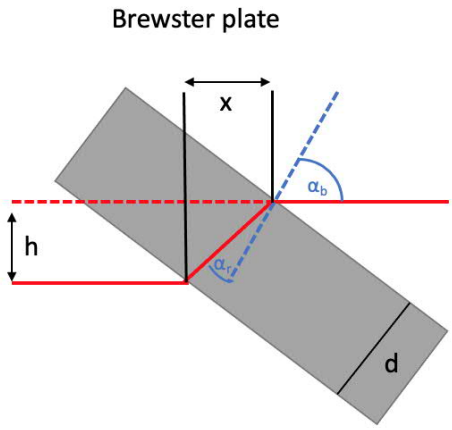

FIGURE 2.9: Schematics of the galvanometer driven Brewster plate.

Frequency control is achieved with a servo loop and a reference cavity. After an output coupler, the beam splits into three beams. 900-1000 mW are transmitted as output light. The other two beams are reflected into the reference cavity. Two photodiodes generate voltage signals into a differential amplifier. If a frequency shift changes the transmission through the cavity an error signal is generated. The servo loop uses that error signal derived from the reference cavity. One part is applied to the M3 mirror (tweeter) to correct fast frequency drifts and the other rotates the Brewster plate for slower cavity length changes.

2.3 Experimental Determination of the Lasersystem

In the following, the RDL parameter for the beam divergence is obtained. The frequency stabilization is explained and the different possibilities are tested and compared.

2.3.1 Laserpower with the Millenia eV 15 as Pumplaser

Because the laser has been upgraded with new components such as the dye pump from Sirah, the performance data given in the manual is no longer reliable. All parameters are obtained using the Rhodamine 6G dye at 578 nm (dye maximum). After a completely new alignment of all-optical parts for lasing and the angle of the dye jet, the RDL achieved an output power of 1350 mW. After inserting the thick and thin etalon as well as the Brewster plate, the power after the output coupler achieved 1000 mW.

2.3.2 Beam Divergence of the RDL

The quality of the laser beam is described by several parameters, which are important for choosing the correct laser for spectroscopy. The focus-ability can be described with the beam divergence Θ. Θ indicates an increase in beam diameter or radius with distance [3].

In the first approach, the RDL is fiber-coupled to achieve a single mode beam. The power of the beam is reduced with an absorption filter and aligned onto an Ophir SP920s Beam Profiling Camera with a chip size of 7.38 x 7.38 mm.

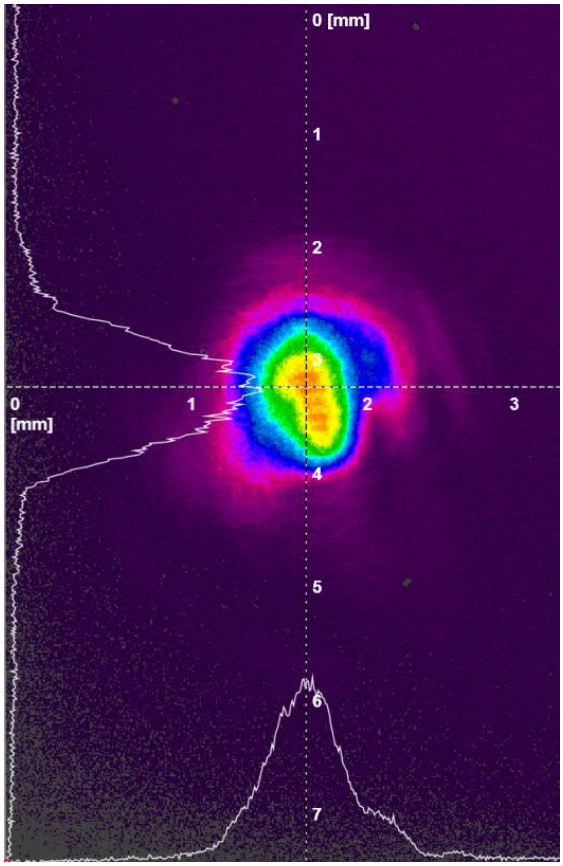

FIGURE 2.10: Beamcamera picture of the RDL.

At a wavelength of 578 nm, the optical boundaries of Fig. 2.10 give a beam diameter d of 1.04 mm, 20 cm after the fiber. Confirmation of the result was obtained by measuring the beam diameter according to ISO 11146 [26]. For this purpose, the diameter of a movable aperture was changed to achieve transmission of 86.5 %. This results in a beam diameter d of 1.05 mm, 20 cm after the laser.

The beam divergence Θ is measured by comparing the beam diameter of two points with distance $l = 10\,\text{cm}$ and the same power on a Thorlabs PM400 power meter. This results in diameters of $d_1 = 1.45\,\text{mm}$ and $d_2 = 1.6\,\text{mm}$ can be calculated with eq. 2.6 [3].

$$\Theta = \frac{d_1 - d_2}{2l} = \frac{1.6 - 1.45[\text{mm}]}{2 \cdot 0.1[\text{m}]} = 0.75\,\text{mrad} \tag{2.6}$$

2.3.3 Frequency Stabilization

Many spectroscopy experiments rely on frequency-stable lasers. Therefore the laser has to be locked onto one specific frequency. Since many lasers already come with electronic components for locking and scanning, new technologies have emerged to achieve better stability results. In the following the internal laser locking and scanning is compared to an active laser stabilization with a Helium-Neon (He-Ne) reference laser. The He-Ne also calibrates the High Finesse WS-8 wavemeter, where all upcoming experiments are obtained. First of all, there will be a closer look at the He-Ne laser, followed by a comparison of the frequency stabilization possibilities of the RDL.

2.3.3.1 He-Ne Laser

A.Javan, W. R. Bennett, and D. R. Herriott observed laser operation from an electric discharge in a mixture of helium and neon gases in December 1960 [27]. This invention was not only the first gas laser but also the first laser that operated continuously. Nowadays gas lasers are divided into neutral atoms-, ion- and molecule-laser.

The active medium is excited through electrical discharge or with optical pumping. This results in free electrons and ions, which experience acceleration in electric fields but only the free electrons are responsible for the excitation. The low-pressure discharge allows a continuous discharge of the free electrons and gives a Maxwell-Boltzmann distribution. Therefore this technique is set to operate gas lasers in a continuous wave mode.

The resulting kinetic energy of electrons after the discharge leads to collisions with other gas particles. These inelastic collisions transfer energy and excite the gas particles to higher states. If there is only one gas involved a direct excitation takes place. A gas mixture can transfer energy between the two particles Helium and Neon. If the excited

states of the particles collide and a so-called resonance energy transfer takes place, the energy difference ΔE can be smaller than the thermal energy $E = kT$. This case gives a probability that one atom stays in the excited state and the other one decays into the ground state.

This collision transfer is important when the atoms are in a metastable state as a consequence of a forbidden transition. It still can be used as an energy reservoir for the other atom. Next, to these two effects, the molecules can also decay to ground state via stimulated or spontaneous emission or collisions with setup limitations like a tube wall. This restricts the population inversion in comparison to a dye or solid-state laser. Therefore a partial pressure is used to control the excitation of the higher states. As mentioned in 1.2.2 the laser excitation rates and the lifetimes of the levels are important to generate a population inversion. Especially the lifetimes are a basic condition to achieve continuous lasing in a gas laser [13, 28]. There will be a closer look at the structure and physical principles of the He-Ne Laser.

Since the invention in 1960, the He-Ne Laser nowadays is used at a stable visible 633 nm emission line of Neon. The helium is mixed 1 : 10 to Neon and works as an energy reservoir mentioned earlier. After a direct current discharge, the characteristic first states to be excited are 2^3S_1 and 2^1S_0. These states are metastable and the optical transitions to the ground state 1^1S_0 are not allowed, because it would violate the selection rules. Then the excited helium atoms collide producing a population inversion in the neon system. This is guaranteed through the approximately ten times higher longer lifetimes of the s-states. The $2p$-state decays within spontaneous emission into the $1s$-state. There the atoms accumulate because of the 100 ns lifetime and collide with the discharge electrons. This leads to an excitation back to the $2p$-state reducing the population inversion for stimulated emission. Through collisions with the tube wall the atoms reach their ground state. The diameter of the tube wall is therefore connected to the amplification of the laser transition. A small diameter will reduce the collisions with the tube wall but will also lower the laser power. Therefore an optimum for these contradictory conditions has to be found which gives the characteristic stable but low power output of a He-Ne laser [7, 17].

Today's constructions of He-Ne lasers consist of a laser tube made out of glass. Surrounded by housing, the gas discharges are operated with an external or internal power

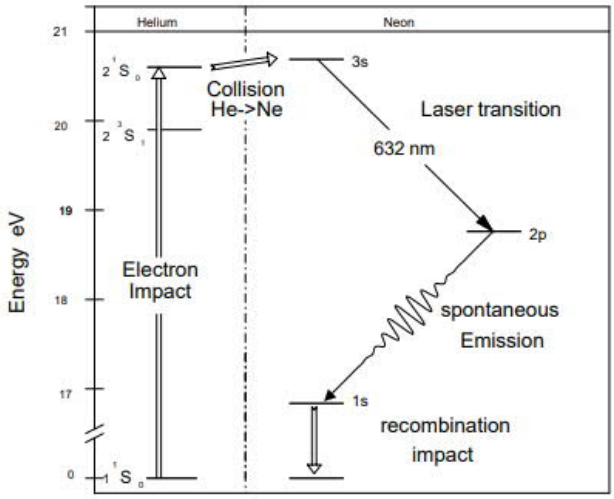

FIGURE 2.11: Energy level diagram of a He-Ne laser.
Reprint from [7]

supply unit. On the inside is a Brewster window, where parallel polarized light has no reflection loss and an oscillation is enabled.

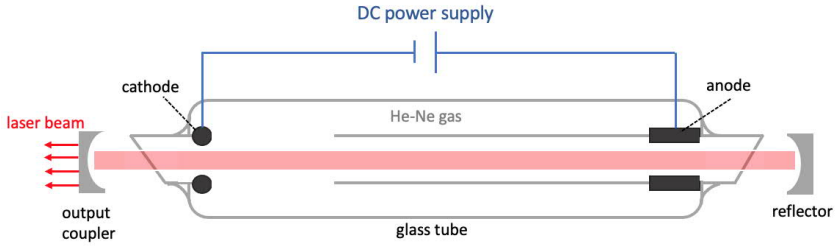

FIGURE 2.12: Schematics of a He-Ne laser.

2.3.3.2 Feed Forward for Locking and Scanning

The RDL consists of a control box to internally lock and to scan the frequency of the laser and an additional reference cavity. The reference cavity sends an error signal depending on the operation mode of the laser. On the front panel, the frequency can be changed through a thin etalon offset and a manual scan knob. The operation mode can be switched between lock, free run, and zero servo for calibration. To successfully control the laser a feed forward alignment to the control box has to be done. Together with an oscilloscope, the resistors of the main scan components are changed to reference signals specified by the manufacturer. This leads to the adjustments of the reference cavity, Brewster plate, and thick and thin etalon.

2.3.3.3 Active Laser Stabilization

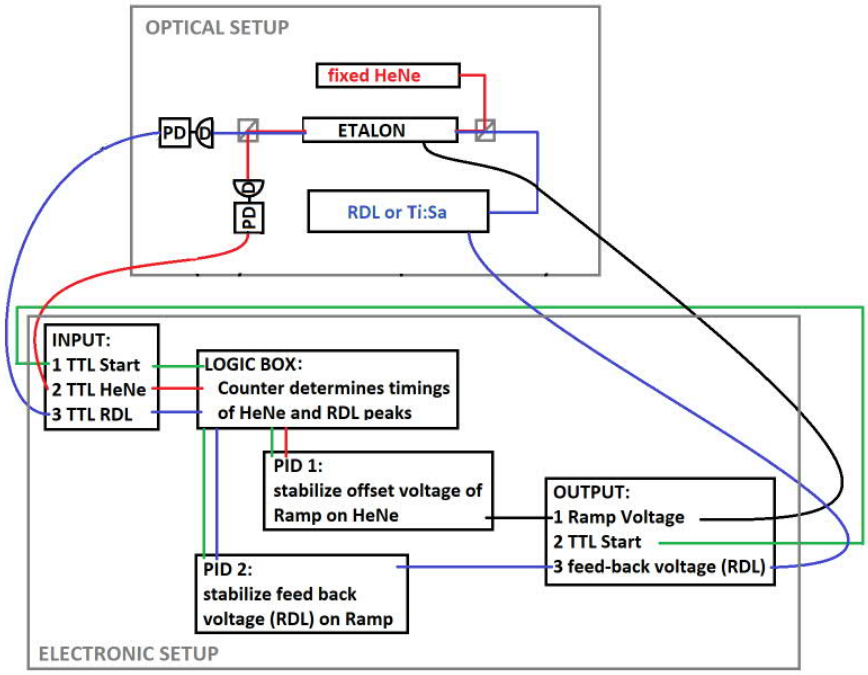

FIGURE 2.13: Optical setup of the active laser stabilization.

The goal is to actively stabilize the RDL, which drifts in frequency relative to a very stable frequency of the He-Ne laser at a repetition rate of 100 Hz. The optical setup Fig. 2.13 shows the arrangement of the lasers. Both laser beams are guided into a Fabry-Perot interferometer using beamsplitters and waveplates. These are polarization separated (90 degrees to each other) and detected via two photodiodes. These signals are processed in an electronic setup, whose hardware consists of a field-programmable gate array (FPGA) operating in real-time and a CPU. The software has been written in LabVIEW by co-workers of the FHI electronics lab.

On channel 1 of the electrical setup, the output signal consists of a voltage ramp and a proportional-integral–derivative-controlled (PID) offset voltage. These operate the scanning etalon. The ramp voltage tilts the etalon and under certain tilt angles, the light of the lasers is transmitted into the two photodiodes. With peak detection, the signal is transferred over to the electrical setup. Because there are several transmissions per laser on the rise of the voltage and the drive back, adjustable registers are installed to hide unwanted transitions. A TTL trigger pulse gives the start and the end of the linear ramp voltage. The procedure is divided into three phases. Phase one rises the

ramp voltage linear from the entered start to the end value. This phase starts after the *high* to *low* transition of the TTL trigger pulse. Phase two is the voltage drive back, where the voltage falls linear until the start voltage. Phase three holds the voltage to recover the etalons. A differential amplifier is used to raise the output voltage from 10 V to 100 V, which is the operating voltage of the built-in etalons.

The electronically determined transmission times and the software set times are used to control the offset voltage of the ramp on channel 1 utilizing PID control. On channel 2 these times are used to set the RDL frequency on a certain setpoint of the ramp voltage. The PID control, transmission, software times, and voltage values can be set via LabView software [29].

2.3.4 Comparison of the Frequency Stabilization for Spectroscopy

To compare the stabilization the RDL is aligned onto a photodiode and scanned with LabView software. The amount of 10000 counts correspond to a frequency interval of 300 MHz or of 0.01 cm^{-1}. Since the output power of the dye depends on its exciting frequency, the signal on the photodiode gives a direct comparison to the stability of the frequency. The RDL is scanned three times over a range of 10000 counts with a step size of 100 counts and resulting in 100 data points. Next to the optical improvements the evaluation of the data shows a better stability, with the same standard deviation of the signals. Therefore the active stabilization is used in the following experiments, providing a total scan range of 2.4 GHz. The laser peaked at a maximum power of 750 mW at this time. One disadvantage of active stabilization is its high power dependency. For an error-free scan, the laser requires a power of at least 600 mW. Otherwise, the signal is too small for the Fabry-Perot interferometer, and errors in the software occur.

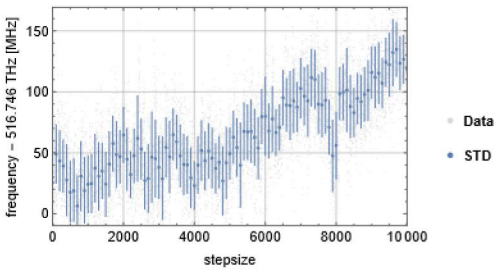

(A) Frequency stability of the RDL in Freerun mode.

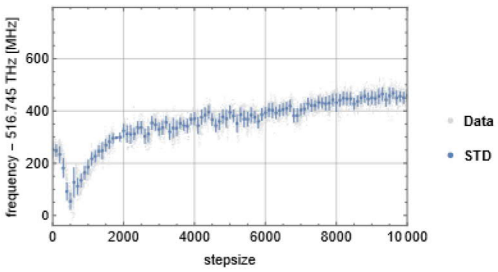

(B) Frequency stability of the RDL in Freerun mode.

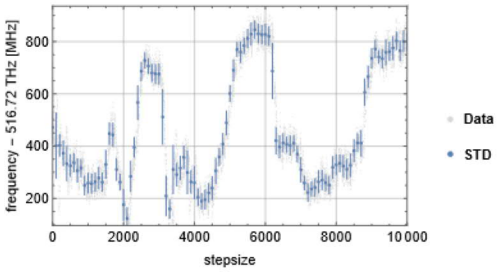

(C) Frequency stability of the RDL in Freerun mode.

FIGURE 2.14: Comparison of the RDL frequency scanning, operating the RDL in Freerun mode (A,B,C). Grey represents the signal from the photo diode and blue is the standard deviation of 100 steps.

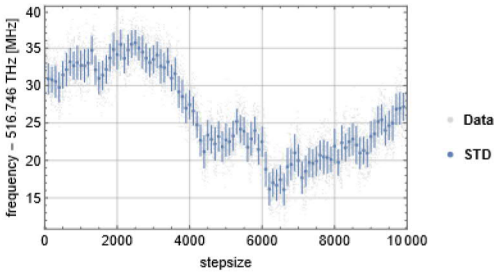

(A) Frequency stability of the RDL with the internal Lock.

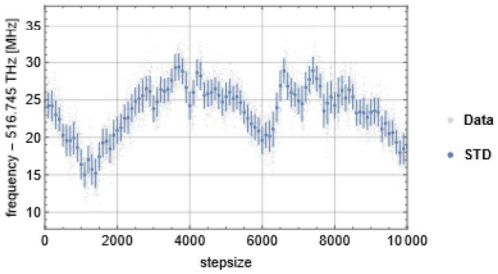

(B) Frequency stability of the RDL with the internal Lock.

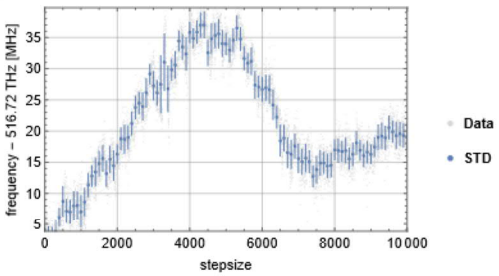

(C) Frequency stability of the RDL with the internal Lock.

FIGURE 2.15: Comparison of the RDL frequency scanning, operating the RDL with an internal Lock (A,B,C). Grey represents the signal from the photo diode and blue is the standard deviation of 100 steps.

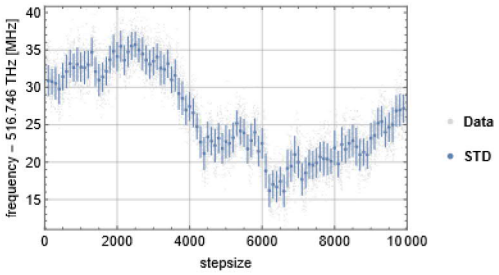

(A) Frequency stability of the RDL with the active stabilization..

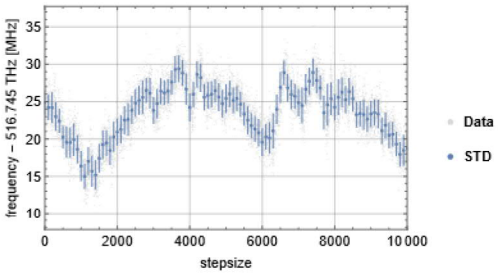

(B) Frequency stability of the RDL with the active stabilization.

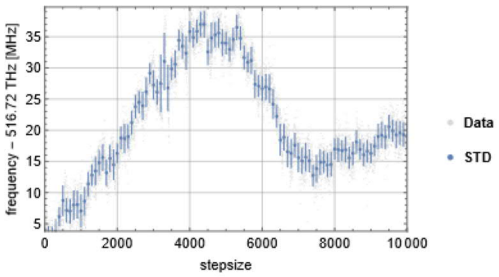

(C) Frequency stability of the RDL with the active stabilization.

FIGURE 2.16: Comparison of the RDL frequency scanning, operating the RDL with an active stabilization (A,B,C). Grey represents the signal from the photo diode and blue is the standard deviation of 100 steps.

The data obtained from Fig. 2.14, Fig. 2.15, and Fig. 2.16 can be seen and compared in the Tab. 2.1. The data shows an improvement of the stabilization alignment with the active frequency stabilization unit.

TABLE 2.1: Experimentally comparison of the active and internal frequency stabilization

Freerun			
Difference Max-Min [MHz]	248.07	516.26	876.63
Standard deviation [MHz]	51.26	98.44	245.63
Lock			
Difference Max-Min [MHz]	24.59	18.24	38.65
Standard deviation [MHz]	5.92	3.99	8.92
Active stabilization			
Difference Max-Min [MHz]	2.49	2.84	3.1
Standard deviation [MHz]	1.07	1.07	1.25

After realignment of the laser cavity, compare section 2.3.1, 30 percent more output power was achieved. With the collaboration of the FHI electronics lab, the software was improved. The repetition rate can now be changed manually from 100 Hz to 50 Hz and 25 Hz. With a stepsize from 20000 counts to 320000 counts, the RDL can now be scanned up to 10 GHz. Since this stabilization is used for the high-resolution scans and the Lamb-dip experiment, a long-term scan is recorded to determine the jitter. Fig. 2.17 shows the new aligned scan, where the jitter is obtained by subtracting a linear model. This results in a jitter of 1.5 MHz at the smallest possible step size of 100 (which corresponds to 3 MHz) and a moving average of 100.

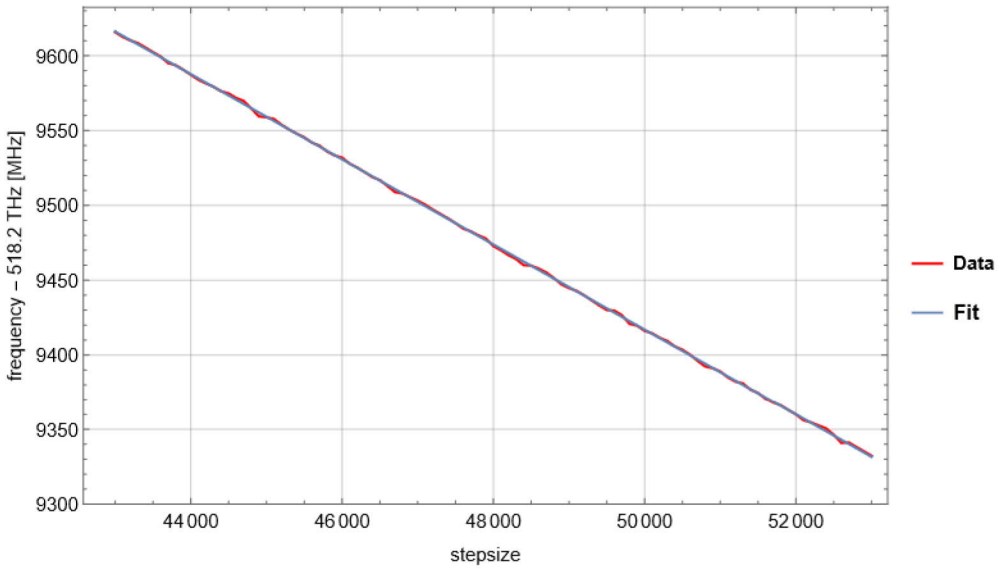

(A) Frequency scan of the RDL (Red) with the a linear model (blue)

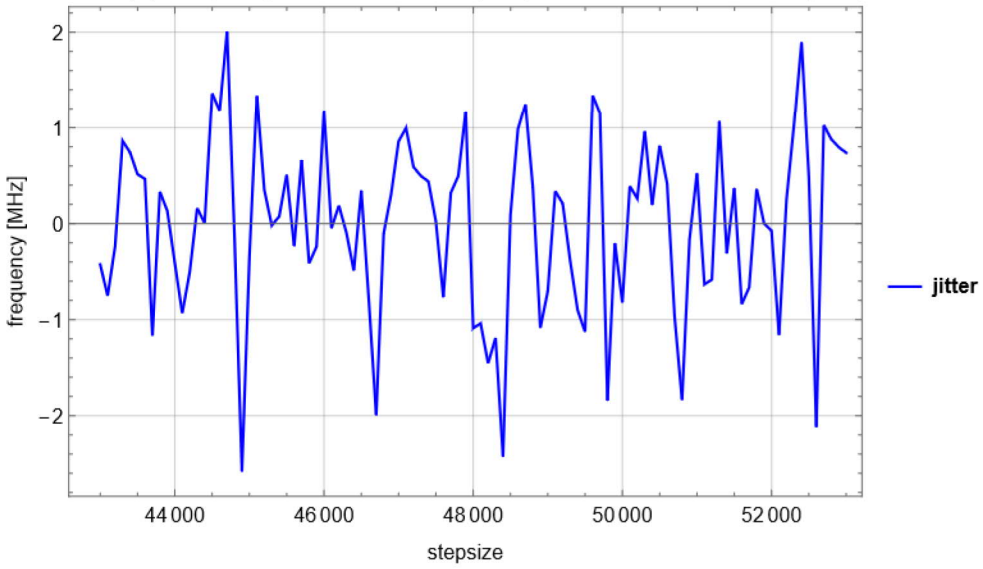

(B) Obtained jitter after subtracting a linear model with a root means square of 1.5 MHz

FIGURE 2.17: Obtaining the jitter from a RDL scan.

Chapter 3

Continuous Ring Dye Laser to seed a Pulsed Dye Laser System

After ensuring the frequency stabilization and scanning of the RDL works, the laser output is used to seed a pulsed dye amplifier (PDA). In this chapter, there will be a closer look at the PDA and how the characteristics of a Brillouin scattering frequency shift (SBS-shift) can be a disadvantage. The shift is experimentally determined with various measurements methods.

3.1 Pulsed Dye Amplifier low Repetition Rate

Sirah Lasertechnik's PDA generates high-energy pulses once seeded with a cw laser. The resulting laser pulse has the frequency of the seed laser and the pulse duration of the pump laser which is injection seeded. Fig. 3.1 shows the optical layout of the PDA system: it has five amplification stages and a phase conjugate mirror based on stimulated Brillouin scattering (SBS). These produce single-mode laser pulses by suppressing the seed laser beam and spontaneous emission. The amplification stage is realized by two circulator systems with rectangular dye cells. An additional circulator with an amplifier cell completes the PDA [8].

In addition to active frequency filtering, the SBS-cell showed the disadvantage to cause a frequency shifting (SBS-shift). The design and shift are determined in the next section.

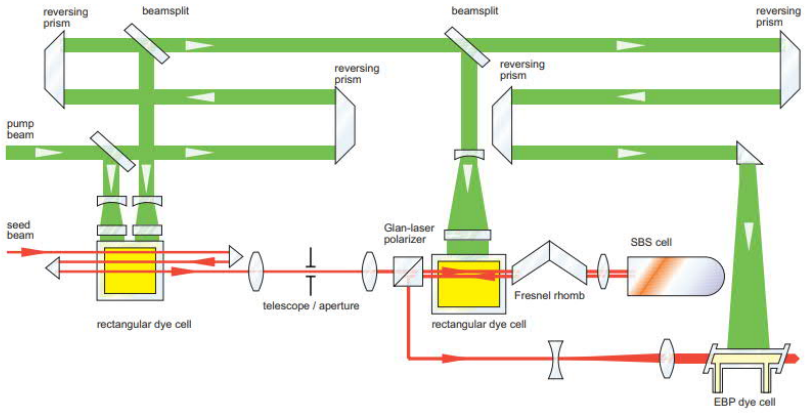

FIGURE 3.1: Schematics of the PDA.
Reprint from [8]

3.1.1 Brillouin Scattering and Shift

The Brillouin scattering is a light-matter interaction, where light-induced density fluctuations cause a modulation of the refractive index which in turn are responsible for scattering. These fluctuations propagate with the velocity of sound and are attributable to the thermo-elastic motion of molecules. The motion can be described as a superposition of spatial and temporal waves causing a refractive index modulation that results in a diffraction of the incoming wave. If the density modulation moves towards the incoming wave, the scattered waves experience a Doppler shift. This effect is divided into stimulated Brillouin scattering (SBS) if the origin of the density modulation is the incoming wave. Otherwise, it's called spontaneous Brillouin scattering. The incoming photon is annihilated, creating a new frequency-shifted photon and phonon. Even small intensities trigger a SBS, which also shows to possess a threshold: once it is exceeded, the signal power and hence the back-scattered intensity can not be increased [30].

The SBS self-pump process is achieved by focusing a laser beam into the SBS medium, with a wavelength λ_i, frequency ν_i and wave vector $\vec{k_i}$. The light propagates through an acoustic wave with wavelength λ_a, frequency ν_a and wave vector $\vec{k_a}$. The acoustic wave causes a refractive index modulation which can be contemplated as refractive grating. The incident light is scattered when it satisfies the Bragg condition, with θ as a scattering angle.

$$2\lambda_a \sin(\frac{\theta}{2}) = \lambda_i \tag{3.1}$$

Since the acoustic wave is moving with a velocity v, the frequency of the scattered light ν_s is Doppler shifted. A detailed explanation of the Doppler shift can be found in section 6.3. The ν_s can be obtained with:

$$\nu_s = (1 \pm 2\frac{vn}{c}\sin(\frac{\theta}{2})) \cdot \nu_i = \nu_i \pm \nu_a \tag{3.2}$$

with n being the refractive index and c being the speed of light. The frequency shift of the scattered light $\|\nu_i - \nu_s\|$ is identical to ν_a. The algebraic sign depends on the direction of the incident light propagating relative to the acoustic wave. If both waves propagate in the same direction this results in a negative sign. The frequency shift also depends on the scattering angle θ with a maximum for backward scattering $\theta = 180°$. The SBS-shift has different ranges for backward scattering, with several hundred MHz for species in the gas phase and a GHz range for liquids and solid-state matter [31].

3.1.2 SBS-Cell Design

The SBS-cell consists of an active SBS-fluid, reflecting only the single mode radiation above a certain threshold. It works as an active filter for spontaneous emission, cw- and pulsed multimode, and cw single-mode radiation. Single mode pulses are reflected with a threshold over 1 mJ and a reflectivity of 40-45 %. Next to the filtering process, the reflected light gets frequency shifted. According to Sirah Lasertechnik the SBS-shift is frequency independent and constant at 1.85 GHz [8]. To get a better understanding of the SBS-fluid and its properties, there will be an experimental verification of the SBS-shift. First there will be an overview of the chosen seed and pump lasers.

3.1.3 Nd:YAG as Pump Laser

ND:YAG is an abbreviation for Neodymium:Yttrium-Aluminum-Garnet. It's a synthetic crystal doped with neodymium ions, which works as a laser medium for solid-state lasers. The four-level system allows lasing in continuous and pulsed mode.

Neodymium has an emission wavelength near 1 μm, but there are several possible laser transitions in the near-infrared and near-ultraviolet. A change of the host environment

(YAG) causes differences in lasing characteristics with effects on radiative transition strength, radiationless decay, and excited state absorption [32].

Although the effects of different host environments on the spectroscopic properties of Nd^{3+} are more subtle than those for transition-metal ions, they can cause significant differences in lasing characteristics through changes in physical processes such as radiative transition strength, radiationless decay probabilities, excited-state absorption, and cross-relaxation quenching.

The power output of the laser is generated and controlled with a Q-Switch. By changing the trigger times for the flash-lamp and the Q-Switch, the power can be maximized or controlled. Because of its high stability and power output, Nd:YAG lasers are selected as a pumping source for the PDA.

3.1.4 RDL and Ti:Sa as Seed Lasers

Both lasers are used to seed the PDA to reach specific wavelengths. The second harmonic of a Matisse 2TR Titan:Sapphire (Ti:Sa) cw laser is used to drive the $a \leftarrow X$ transition in AlF at 367 nm. The construction of the laser is very similar to the ND:YAG, since both lasers are solid-state lasers. The exact schematic can be seen in Fig. 3.2. Two curved mirrors focus the light on a Titan:Sapphire crystal. The additional optical elements, etalons, birefringence filter, and the reference cavity allow wavelength tuning and frequency locking very similar to the RDL. This leads to a high beam quality and an output of nearly 1 W at 733 nm [9]. The RDL seeds a similar PDA to drive various $b \leftarrow a$ transitions of AlF around 578-580 nm. The resulting linewidth is 200 MHz.

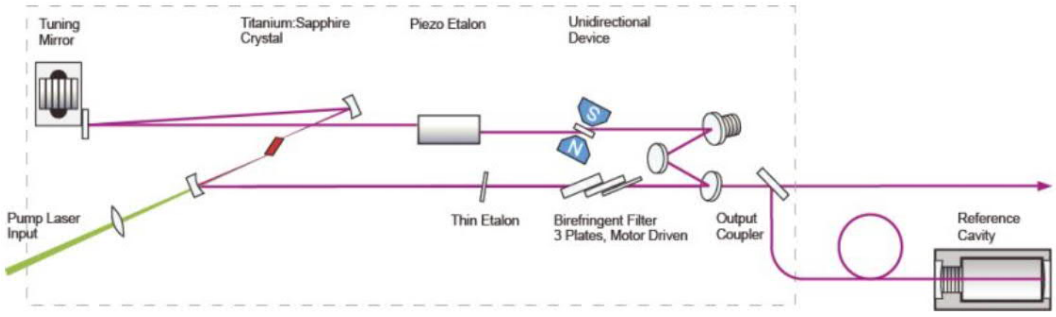

FIGURE 3.2: Schematic of the Matisse 2TR Titan:Sapphire (Ti:Sa) cw laser. Reprint from [9]

3.2 Experimental Classification of the SBS-Shift

To measure vibrational resolved and high-resolution spectra, the SBS-shift must be known perfectly. In this section, different approaches are presented to experimentally define the SBS-shift.

3.2.1 SBS-Shift with Iodine Absorption

Iodine is a diatomic molecule with attractive properties to test experimental techniques. With its bright fluorescence spectrum of numerous lines covering a large part of the visible spectrum and relatively long lifetime in the excited state B which in turn results in narrow spectral lines, it is suitable for many optical and spectroscopic observations [33]. Since iodine absorbs light in the range of 13000-19000 cm^{-1} [34], the range in the following measurements are selected near the expected v-v bands of the $b \leftarrow a$ transitions of AlF. For the experimental observation, two semi-reflective windows split the RDL beam into three separate beams. One weak beam is coupled into a wavemeter (High Finesse WS-8). The second weak beam is pointed through the iodine cell onto a photodiode. The strong beam is amplified and pulsed using the PDA. The power is reduced due to a wedge and guided counter-propagating through the iodine cell and onto another photodiode. The output voltages of the three photodiodes are recorded by a 500 MHz digitizer card.

Three spectra are recorded at 17236 cm^{-1}, 17286 cm^{-1} and 17327 cm^{-1} to determine a possible frequency dependency. In the following there will be a closer look of the evaluation of the absorption spectrum at 17286 cm^{-1}. The frequency axis under the spectra shown in Fig. 3.3 and Fig. 3.4, is the frequency of the cw seed laser.

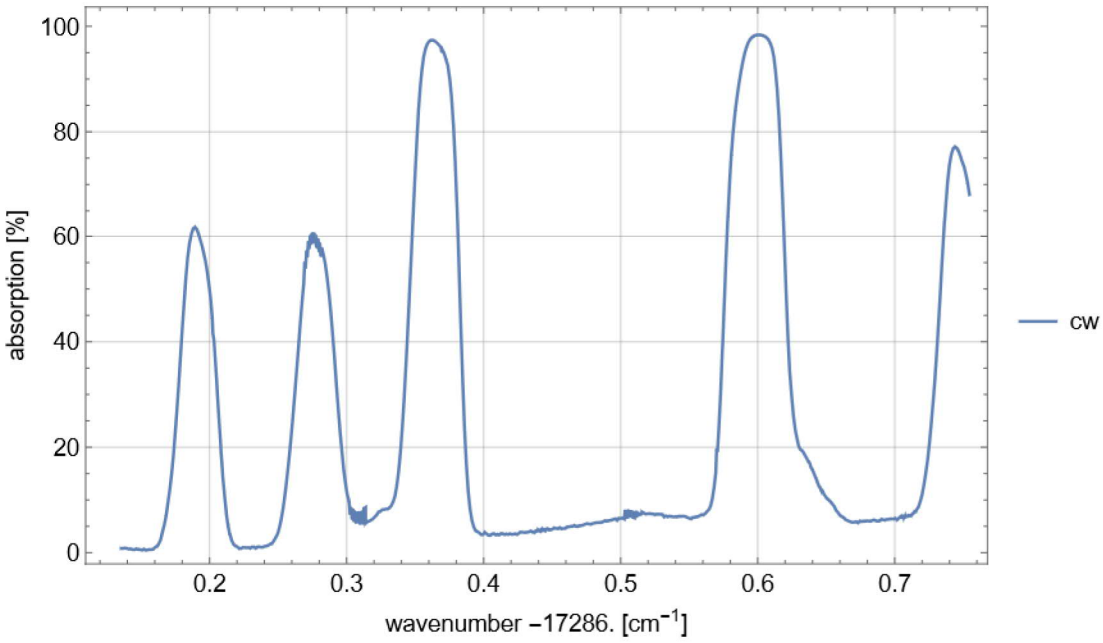

FIGURE 3.3: Iodine absorption spectrum with a cw RDL.

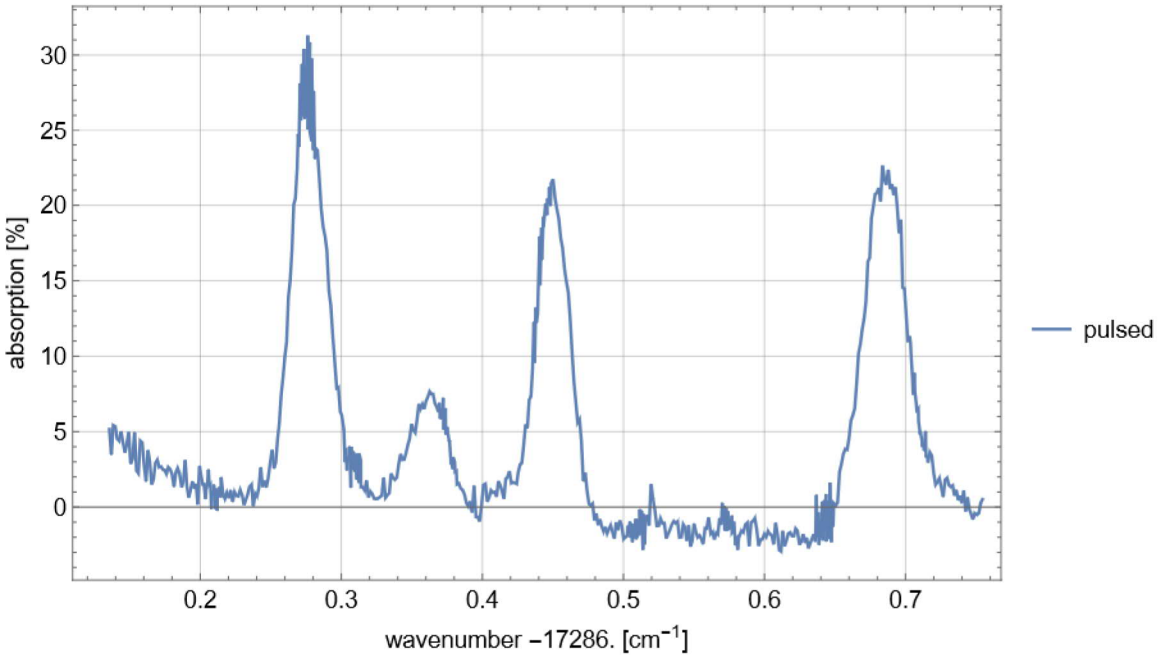

FIGURE 3.4: Iodine absorption spectrum with a PDA, plotted over the frequency of the cw RDL.

The measured spectrum shows more peaks than given in [34]. Later updated versions [35] with smaller intensity peaks completed the atlas. This ensures there is no pollution inside the iodine cell. The spectra lines of iodine in [35] have a fixed frequency. Fig. 3.4 shows the same iodine line at a higher frequency than in Fig. 3.3, which means that the

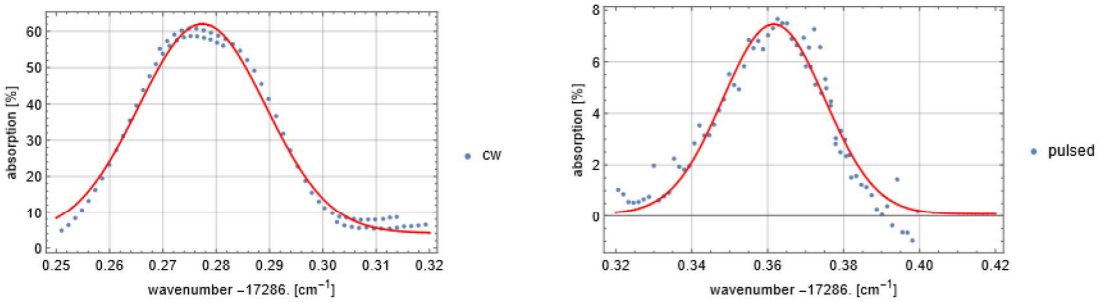

(A) Cw absorption spectra with fit (B) Pulsed absorption spectra with fit

FIGURE 3.5: Example for the Gaussian Fit for the experimental determination of the SBS-shift. On the left side is the cw spectrum (blue) with the Gaussian model (red). The selected peak is the first absorption from 3.3. The right side shows the same peak for the pulsed spectrum (blue) with the Gaussian model (red).

SBS-shift is negative. To determine the SBS-shift a Gaussian function is fit to the three peaks of the cw and pulsed spectra, respectively.

The minimum from all peaks is calculated given the following values. The values are rounded in Table 3.1. The calculated SBS-shift is without this acceptance. A wavemeter uncertainty of 1 MHz is added at the end and the uncertainty is determined by the optical overlap possibilities and Gaussian propagation of uncertainty.

TABLE 3.1: Experimentally measured minimum of the iodine absorption at 17286 cm^{-1}

Peaks	cw [cm^{-1}]	uncertainty [cm^{-1}]	pulsed [cm^{-1}]	uncertainty [cm^{-1}]
Peak 1	17286.191	± 0.005	17286.277	± 0.005
Peak 2	17286.277	± 0.005	17286.362	± 0.005
Peak 3	17286.364	± 0.005	17286.450	± 0.005

TABLE 3.2: Comparison of the measured SBS-shift of the iodine absorption

RDL [cm^{-1}]	SBS-shift [cm^{-1}]	uncertainty [cm^{-1}]	SBS-shift [GHz]	uncertainty [GHz]
17286	- 0.0851	± 0.003	- 2.552	± 0.09
17236	- 0.0863	± 0.003	- 2.591	± 0.09
17327	- 0.0867	± 0.003	- 2.601	± 0.09

Since the Gaussian fits are not good enough on every absorption line to achieve a trustworthy SBS-shift, the pulsed spectra is shifted towards the cw spectra and the difference is plotted in cm^{-1}.

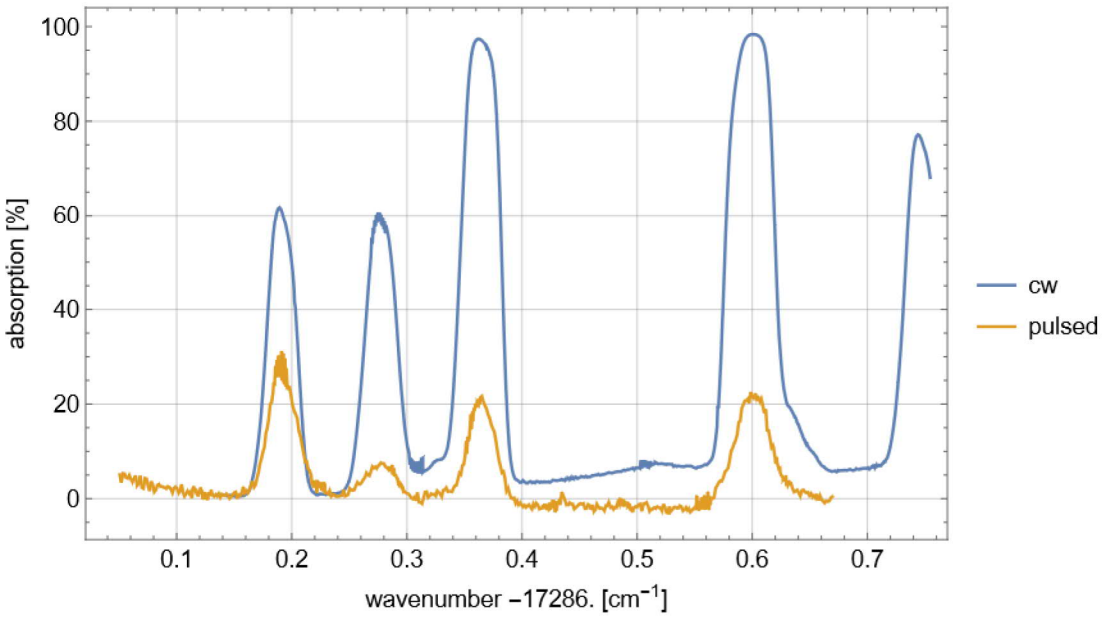

FIGURE 3.6: SBS-shift with optical overlap of 0.085 cm^{-1}. The pulsed spectra (red) is shifted towards the cw spectra (blue).

This leads to the following values. The uncertainty is again determined by the optical overlap possibilities.

TABLE 3.3: Experimentally overlap of the iodine absorption spectra.

SBS-shift at 17286 cm^{-1}	SBS-shift at 17236 cm^{-1}	SBS-shift at 17327 cm^{-1}
- 0.085 cm^{-1} ± 0.003 cm^{-1}	- 0.0865 cm^{-1} ± 0.003 cm^{-1}	- 0.0865 cm^{-1} ± 0.003 cm^{-1}
- 2.55 GHz ± 0.09 GHz	- 2.59 GHz ± 0.09 GHz	- 2.59 GHz ± 0.9 GHz

Since these values are far from the defined absolute 1.85 GHz a comparison with only the High Finesse WS-8 wavemeter is performed. The laser is aligned through the PDA and onto a wavemeter. The accuracy for pulsed laser is a factor of 3–5 smaller than the laser linewidth, which results in 80 MHz [36]. The RDL is frequency locked to 17286.54 cm^{-1} with a jitter frequency of 1.5 MHz. Afterward, the SBS-cell is screened with a mirror. The wavenumber is compared with the cw RDL wavelength, which results in a SBS-shift of - 0.82 cm^{-1} ± 0.0027 cm^{-1} or - 2.46 GHz ± 81 MHz.

3.2.2 Experimental approach of the Frequency Dependency of the SBS-Shift with a Ti:Sa Laser

The results provide an approximate value of the SBS-shift, but no statement can be made about the frequency dependency. After the RDL is limited to a wavenumber range by its dye, a Ti:Sa at about 27000 cm^{-1} is used to excite the $a \leftarrow X$ transition of AlF. The Ti:Sa seeds another identical PDA with a different SBS-cell. The laser is locked to a single absorption line of AlF at 27352 cm^{-1}. A birefringent crystal is used to generate the second harmonic. The detection occurs with (1+1')-REMPI. Detailed insight about the experimental setup can be seen in sec. 4.1. An ion signal is obtained when any order of the SBS-shift is resonant. The fundamental output of the PDA is at $\nu_{seed} - \mathrm{SBS}$, with ν_{seed} as the frequency of the Ti:Sa. The eq. 3.2 shows that also overtones are possible, i.e. the PDA produces also light at $\nu_{seed} - 2\,\mathrm{SBS}$, even though this pulsed energy is lower. Therefore in the spectra, a strong peak at ν_{seed} and a weak peak at $\nu_{seed} + \mathrm{SBS}$ should occur. Since the birefringence crystal doubles the frequency, the SBS-shift is also doubled.

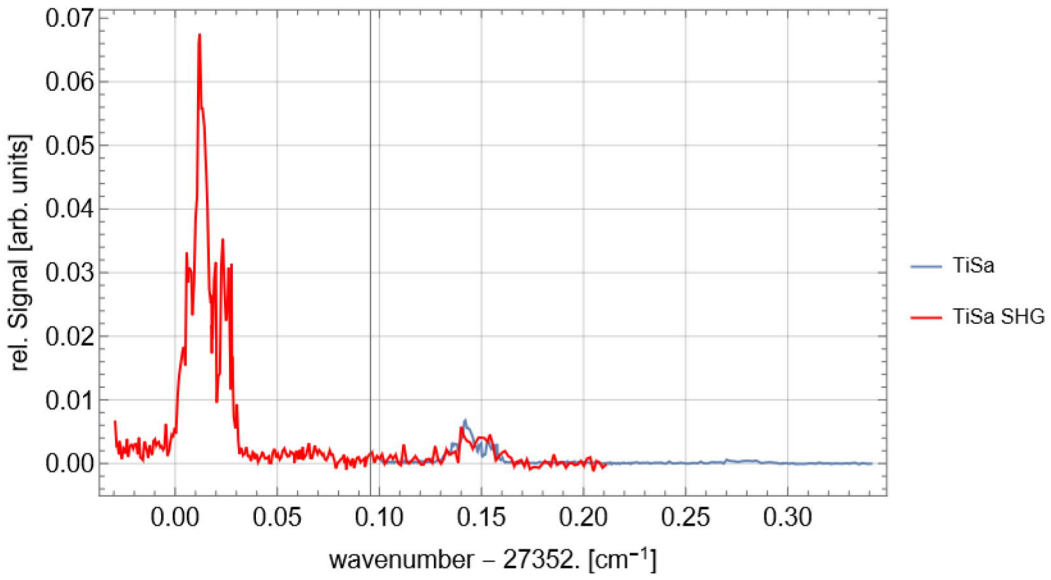

FIGURE 3.7: SBS-shift with optical overlap of a single absorption line of the $a \leftarrow X$ transition of AlF.

Fig. 3.7 shows exactly the expected spectrum. The second-order is resonance with a spacing difference of the SBS-shift. This spacing is calculated leading to a SBS-shift of 0.06472 cm^{-1} $\pm$ 0.001 cm^{-1} or 1.9416 GHz $\pm$ 30 MHz. Since there is no guarantee that the PDAs have an identical SBS-cell, no precise statement can be made about the

frequency dependency. However, it confirms the deviation of 1.85 GHz and thus leads to the conclusion that an explicit measurement of the value should be carried out.

Chapter 4

Experimental Devices for Molecular Spectroscopy on Aluminum Monofluoride

The RDL is used to study aluminum monofluoride (AlF) in a molecular beam. The experimental setup can be seen in the technical drawing, Fig. 4.1. The machine is connected to four vacuum pumps,two fore-pumps, and two turbomolecular pumps, to achieve a vacuum of 10^{-7} mbar. AlF in the gas phase is produced using laser ablation with an Nd:YAG. A molecular beam is achieved through supersonic expansion into the experiment chamber. The detection of the molecules is realized with resonance-enhanced multiphoton ionization (REMPI) or laser induced fluorescence (LIF). In this chapter, the framework of the setup and detection methods are described.

4.1 Experimental Setup of the Supersonic Molecular-Beam Machine

4.1.1 Generation of Aluminum Monofluoride

Aluminum monofluoride is produced through a chemical reaction of aluminum (Al) and sulfur-hexafluoride (SF_6).

$$Al + SF_6 \rightarrow AlF + SF_5 \tag{4.1}$$

Al is generated by laser ablation. A pulsed frequency-doubled Nd:YAG at 532 nm hits a rotating aluminum rod, vaporizing the material and forming it into a plasma. Through this process aluminum changes from solid phase to the gas phase. An electric motor rotating the aluminum rod allows that different spots are hit with every laser pulse. SF_6 is available as a pure gas and launched with a solenoid valve. In the experiment, the gas consists of 2 % SF_6 seeded in a noble gas (Neon), as carrier gas. This mixture is obtained and optimized from earlier experiments [15].

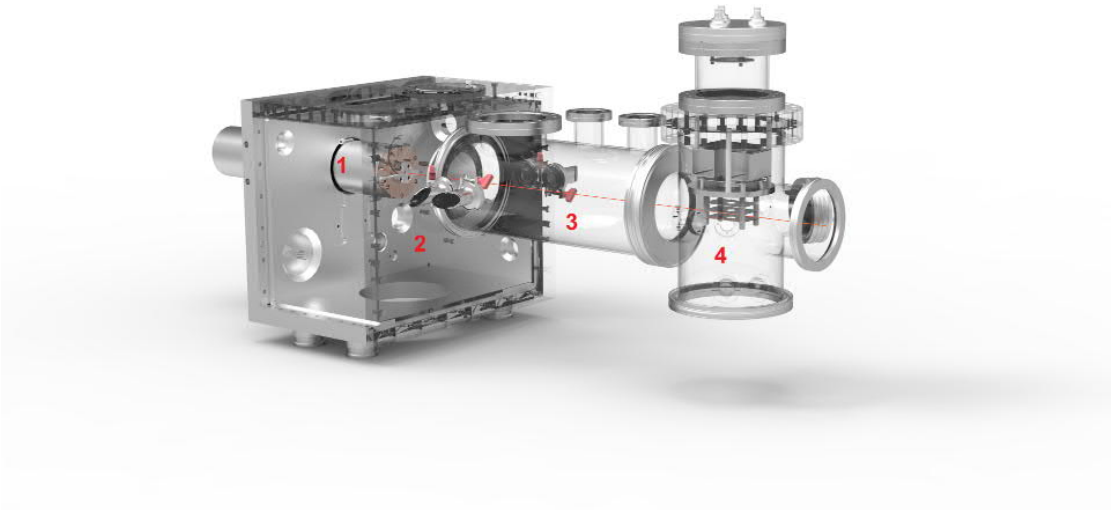

FIGURE 4.1: The supersonic machine.

The solenoid valve (1) with an aperture of d=0.5 mm, is opened and closed with a plunger. A voltage pulse results in a magnetic field to control the plunger and to generate a 50 μs duration gas pulse. Gas that emerges from a region of high pressure through an aperture or orifice into a region of low pressure undergoes a supersonic expansion and leads to a molecular beam [37]. A molecular beam is defined as an accumulation of molecules with the same speed and direction. The beam is termed a seeded molecular beam and is produced in the supersonic expansion chamber (2). Further downstream the beam passes through the propagation chamber, where interaction with radiofrequency or another laser would be possible (3), and finally enters the detection chamber (4) [38].

4.2 Detection Methods

4.2.1 Time-of-Flight Mass Spectrometry of AlF

The complete schematic can be seen in Fig. 4.2. The arrows mark every laser used for detection or excitation. The SHG of a Ti:Sa seeded pulsed dye amplifier at 367 nm is used as a preparation laser for the $a \leftarrow X$ transition of AlF.

A pulsed dye laser from Sirah (PDL) as well as the PDA are operating at the same wavelength. Either one or the other is used to excite the $b \leftarrow a$ transitions of AlF.

In the detection chamber, the AlF molecules get ionized by a pulsed dye laser that crosses the molecular beam perpendicularly. All positively charged molecules are detected with Time-of-flight (ToF) mass spectrometry. Rhodamine 6G provides an output of 560 nm. Afterward, it's aligned to an SHG crystal generating a second harmonic at 280 nm at around 5 mJ. The ToF consists of two electrodes with a potential difference. The resulting electric field accelerates the positively charged molecules towards the extraction grid. The other one is called repeller and has to have a higher potential so that only positive ions are accelerated towards the extraction grid. The molecular beam and laser beam are aligned such that they cross each other between the two electrodes. After ionization, the molecules travel through another grid, which works as a shielding mechanism against the high voltage of the microchannel plate (MCP). The microchannel plate is attached at the end of the chamber as a detector. The plates consist of a variety of tubes coated with lead oxide. The layer is high impedance and works as a voltage divider and secondary electrons emitter. When a single incoming ion hits the microchannel plate, the secondary electrons trigger an avalanche of electrons [39]. The resulting charge impulse at the anode is transferred to a 500 MHz digitizer card.

The excitation and ionization of AlF take place by frequency-doubled lasers. This technique is called Resonance-enhanced multiphoton ionization (REMPI). The number of photons involved for excitation (n) and ionization (m) is specified as (n+m)-REMPI.

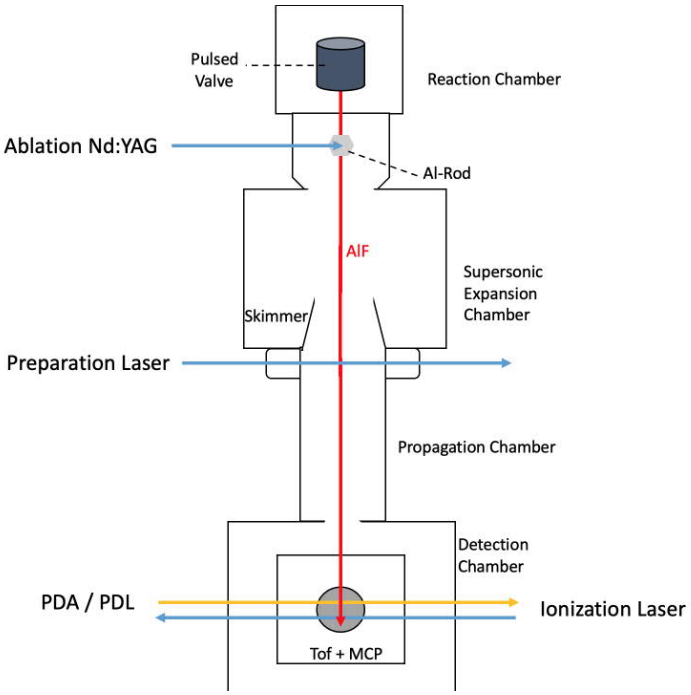

FIGURE 4.2: Drawing of the ToF measurements with lasers.

4.2.2 Laser Induced Fluorescence Detection of AlF

Optionally, a laser induced fluorescence zone (LIF-Zone) can be installed in the propagation chamber (3). The setup is designed by the workgroup of Stefan Truppe [10] and can be seen in Fig. 4.3. When molecules are exposed to a laser beam with a certain intensity I and frequency ν the product of the absorption coëfficient $\alpha^0(\nu)$ and $I(\nu)$ gives the amount of energy absorbed. The emitted photon from the molecule generates the LIF-signal $I_{LIF}(\nu)$ which is proportional to $\alpha^0(\nu)I(\nu)$.

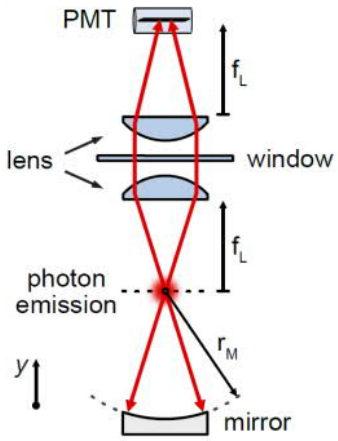

FIGURE 4.3: Schematic drawing of the LIF-Zone
Figure reprinted from [10].

The complete setup used to record the following spectra can be seen in Fig. 4.4. The RDL is aligned through an optical fiber with a maximum output of 20 mW. A beamsplitter cube enables polarization separation, into a perpendicular and a parallel part, and the transmitted/reflected intensity is adjusted with a $\lambda/2$-plate. The parallel polarized light is guided through a slit and into the machine through Brewster windows, to reduce reflection loss.

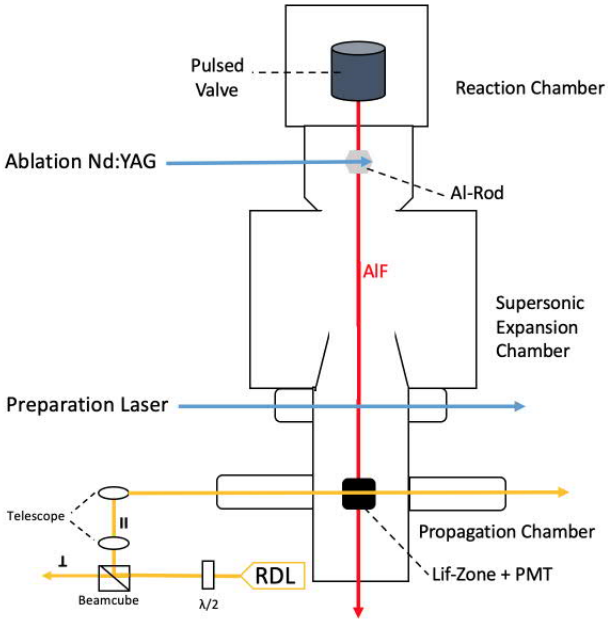

FIGURE 4.4: Drawing of the LIF measurements.

Chapter 5

The Diatomic Molecule Aluminum Monoflouride

In this chapter, there will be a closer look at the properties of a diatomic molecule, with focus on Aluminum monofluoride. Aluminum monofluorides' energy level diagrams is examined.

5.1 Diatomic Molecules

Molecular spectroscopy records the electronic, vibrational, and rotational states of selected molecules. The wavefunction of a state is given by the eigenfunction ψ and the energy of the state is given by the eigenvalue E of the Schrödinger equation [40]. According to Herzberg, the resulting total energy is the sum of the energy of three components:

$$E = E_e + E_v + E_r \tag{5.1}$$

with contributions from the electronic, vibrational, and rotational motion, respectively.

5.1.1 The Electronic States of a Diatomic Molecule

The absorption of a photon causes that one or more electrons are excited from a lower to a higher molecular orbital. Electronic states of molecules involve configuration interactions

and the free electrons in orbitals participate in the total spin S and the total angular momenta L of the state [42]. Singlet (S=0) and triplet (S=1) states differ in their energy because of the anti-symmetry conditions of the wavefunctions. The quantum numbers $\Lambda = |M_L|$ and $\Sigma = M_S$ are introduced to give the absolute values of the projection of L and S on the internuclear axis. States with $\Lambda = 0, 1, 2, 3$ are referred to as $\Sigma, \Pi, \Delta, \Theta$-states. The quantum number for the total angular momentum on the internuclear axis Ω is:

$$\Omega = |\Lambda + \Sigma| \tag{5.2}$$

The notation for the ground state X can be described as follows. The first upper index describes the state (^{1} for singlet) and the other index gives the parity, in this case $X^1\Sigma^+$. An excited state is labelled with a capital letter for states with the same spin-multiplicity than the ground state and with a small letter for different spin-multiplicity. In the official notation, the upper value shows the spin multiplicity and the lower value represents Ω. For example $a^3\Pi_1$ for the $\Omega = 1$ manifold of the triplet state [41].

5.1.2 Nuclear Vibration and Rotation of Diatomic Molecules

5.1.2.1 Nuclear Vibration

A diatomic molecule as a whole has two nuclei that can vibrate relative to each other. This leads to several, more or less equidistant vibrational levels, labeled with the vibrational quantum number v. The frequencies for AlF are in the range of 800-1000 cm^{-1} for all electronic states [38].

5.1.2.2 Nuclear Rotation

The rotation of a diatomic molecule can be simplified by a classical mechanic model of a rigid rotor. The whole molecule rotates perpendicularly around the center of the internuclear axis. With L is the angular momentum and the moment of inertia I, the rotational energy E_{rot} is given by:

$$E_{rot} = \frac{L^2}{2I} \tag{5.3}$$

Since the energy of this system is quantized, the solution for the time-independent Schrödinger equation gives the eigenvalues of the system. By solving the equation of the rigid rotator which can be seen in [42], the resulting energy is:

$$E_{rot} = BN(N+1) \tag{5.4}$$

N summarizes the nuclear rotation and B is the rotational constant defined as $B = \frac{\hbar^2}{8\pi^2 I}$. It can be used to construct a rotational energy level diagram [41]. For all the electronic states of AlF, the value for the rotational constant is about 0.5-0.6 cm^{-1}.

5.2 Aluminum Monofluoride

As mentioned in the introduction, AlF is a good candidate for laser cooling because of its highly diagonal Franck-Condon-Matrix between the $X^1\Sigma^+$ ground state and $A^1\Pi$ excited state. Also a simple hyperfine structure and rotational closed transition are favorable properties of the molecule for the cooling cycle [15]. To get an overview why this molecule is chosen, we take a look at the energy level diagram of AlF.

5.2.1 Energy Level Diagram of AlF

The electronic transitions of gaseous AlF are summarized by the group of Barrow et al. [11] and can be seen in Fig. 5.1. The work is referred to the ground state $X^1\Sigma^+$, the first excited states $A^1\Pi$, $a^3\Pi$ and the second excited triplet state $b^3\Sigma^+$. Temperature in the μK range can be achieved on the spin forbidden $a^3\Pi \leftarrow X^1\Sigma^+$ transition [15]. The Franck-Condon-Matrix is diagonal between the $A^1\Pi$ and $X^1\Sigma^+$ states as well as between the $a^3\Pi$ and $X^1\Sigma^+$ states and the Q-branch transitions are rotationally closed [11, 15].

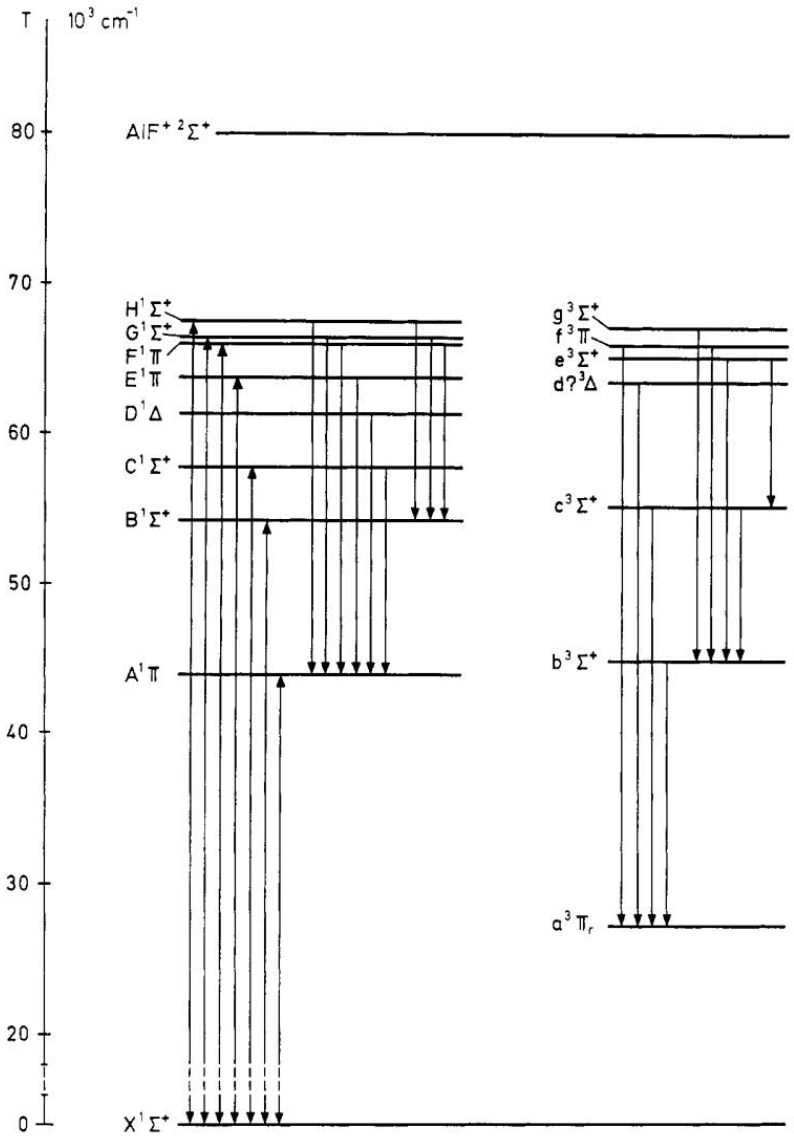

FIGURE 5.1: Electronic states of AlF
reprint from [11].

5.2.1.1 Lambda Doubling

In AlF, Λ-doubling occurs in the $a^3\Pi$ state and is in the range of $0.3\,\mathrm{cm}^{-1}$ for $\Omega = 0$ [15]. This is a splitting effect of every J-level because of the spin-orbit interaction of L and S. It occurs when $\Lambda \neq 0$. The size of the splitting increases with higher J and the order of magnitude is depending on Ω, with its maximum at low Ω [41]. The different Λ-doublet levels have opposite parity, and a common labeling scheme that is used describes these levels as e and f levels, according to:

$$\text{e-levels with parity } p = +(-1)^J \tag{5.5}$$

$$\text{f-levels with parity } p = -(-1)^J \tag{5.6}$$

5.2.1.2 Perturbation of the Electronic States of AlF

Barrow et al. [11] observed a perturbation of the $b^3\Sigma^+, v = 5//A^1\Pi, v = 6$ complex. The lines for low quantum numbers show broadening effects in the vicinity of the perturbation. With an approximation as transitions for the upper three triplet levels and the three lower levels with the same splitting, the interactions show a weakening of lines in unperturbed positions and extra lines near them [11].

Chapter 6

Broadening and Shifting Effects of Spectral Lines

The discrete absorption and emission lines are often referred to as fingerprints of the molecule. These lines are not monochromatic though, there are broadening and shifting effects, which influence the resolution of a spectrum. The following sections give an overview.

6.1 Profile of a Spectral Line

The line profile is not completely narrow and explained by the spectral distribution $I(\nu)$ of the intensity around a center frequency $\nu_0 = (E_k - E_i)/h$ of a molecular transition. Where $\Delta E = E_k - E_i$ gives the energy difference between lower energy level E_i and the upper energy level E_k. The linewidth is characterized as the full width at half of the maximum of the line (FWHM), often shortened with halfwidth [13].

6.2 Natural Linewidth

The spectral profile of a natural broadened absorption line is Lorentzian. The peak is located at the resonance frequency ν_0 and the width is determined by the lifetime of the two involved states. To derive the Lorentzian lineshape the classical model of a damped oscillator can be used. The electrons hovering around the nucleus where

the displacement is proportional to the force on a system. A damping constant γ is considered as the radiative energy loss, t the time, m the reduced mass of the system and ω_0 is the characteristic resonance angular frequency.

$$\ddot{x} + \gamma\dot{x} + \omega_0^2 x = \frac{F(t)}{m} \tag{6.1}$$

For emitted radiation the external force $F(t)$ equals zero. So the equation can be solved as a homogeneous differential equation with the approximation $\gamma \ll \omega_0$, which is justified for molecules. The solution of eq. 6.1 is:

$$x(t) \sim e^{-\frac{\gamma}{2}t} \cos\omega_0 t \tag{6.2}$$

A electron which oscillates with ω_0 is equal to the central frequency of molecular transitions $\omega = (E_k - E_i)/\hbar$.

6.2.1 Lorentzian Line Profile

The FWHM of the Lorentzian distribution is the damping constant γ:

$$\mathrm{FWHM}_L = \gamma \quad \text{with} \quad \gamma = \frac{1}{2\pi\tau_1} + \gamma = \frac{1}{2\pi\tau_2} \tag{6.3}$$

with τ_1 as the lifetime of the excited state and τ_2 the lifetime of the ground state. The sum of the potential and kinetic energy is equal to the time derivative of the total internal energy. Electromagnetic radiation is released when electrons move between different energy levels.The power $P(t)$ of the system is given by:

$$P(t) \sim e^{-\gamma t} \tag{6.4}$$

Eq. 6.4 defines the lifetime τ as the time t when $1/e$ of the inital power is still present in the system, meaning that $\tau = 1/\gamma$. Taken the Lorentzian distribution eq. 6.3 into account the natural linewidth is: [43]

$$\mathrm{FWHM}_L = \frac{\gamma}{2\pi} = \frac{1}{2\pi\tau} \tag{6.5}$$

6.2.1.1 Heisenberg's Uncertainty Principle

The relation of the lifetime and the width of a spectral line can also be acquired by Heisenberg's uncertainty principle. Time and energy are complementary variables and therefore they can only be determined with an uncertainty $\Delta E \sim \hbar/\Delta t$. The transition from an excited state to the ground state has the following angular frequency $\omega_{ki} = (E_k - E_i)/\hbar$, which leads to an uncertainty of:

$$\delta\omega = \Delta E_k/\hbar = 1/\tau_i \tag{6.6}$$

A goal of high-resolution molecular spectroscopy is to achieve a resolution with only the natural linewidth to get exact results. Several broadening effects have to be taken into account by observing molecular spectra.

6.3 Doppler Broadening and Shifting

Assume molecules or atoms in a gas traveling in a certain direction $+z$ with the velocity $\vec{v}$. After interacting with a wave in either the $+z$ or $-z$ the molecule decays, emitting radiation. This radiation has a central frequency of ω_0 but an observer receives the Doppler-shifted frequency ω_D with the wave vector $\vec{k} = \frac{2\pi}{\lambda}\vec{e}_z$:

$$\omega_D = \omega_0 \pm \vec{k} \cdot \vec{v} \tag{6.7}$$

The shift is positive when $\vec{e}_z = +$ with $\vec{k} \cdot \vec{v} > 0$. This effect is also a part of the absorption process of molecules. Where the direction of a moving molecule shifts the frequency higher when moving in the same direction.

Next to the shift, there is also a broadening effect that has to be reconsidered. It has a Gaussian line broadening and can be described via the Boltzmann distribution of an ideal gas. Inserting these relations into the Doppler width:

$$\mathrm{FWHM}_D = \omega_0 \sqrt{\frac{8RT \ln 2}{mc^2}} \tag{6.8}$$

with R as the gas constant, m as mass, and c as the speed of light. This shows an dependency of the temperature T in Kelvin [44].

To reduce these broadening and shifting effects there are several possibilities that are applied in the laboratory. The main considerations are the use of translationally cooled molecules and the right alignment of the laser beam to the molecular beam. The supersonic source lowers the temperature of the molecules. Many apertures help to achieve a perpendicular alignment of the two beams.To block diverging molecules, skimmers and vertical slits can be attached after the source [13, 45].

6.4 Collisional Broadening

So far we have viewed atoms or molecules without any interactions among them. When two atoms approach another, a collision results in a shift depending on the electron configuration and the distance of both partners. The line shift $\delta\omega$ caused by elastic collisions corresponds to an energy shift of an atom and the photon energy, which means the kinetic energy sinks with a positive shift $\delta\omega > 0$ and is defined as:

$$\delta\omega = \gamma_n + \gamma_{coll} \tag{6.9}$$

If any excitation energy is transferred into internal or translation energy the collision is called inelastic. They decrease the number of excited atoms to an level E_k which suppresses the fluorescence intensity. A Lorentzian profile arises for the line broadening by inelastic collisions and the FWHM depends on pressure p and temperature T leading to:

$$\mathrm{FWHM}_C = \zeta p \left(\frac{T}{T_0}\right)^{\eta} \tag{6.10}$$

where ζ and η are molecule specific parameters depending on the gas mixture. The advantage of using a supersonic source restricts the collision broadening effect in the

following experiments, because it reduces the density of the molecules and has a slim velocity distribution.

6.5 Laser Profile Broadening

When molecules passing through a laser beam, the transit time $T = d/|v|$ can be shorter than the lifetime of those levels. These interactions set the limits for the linewidth by the time of flight from a molecule through the beam. The profile of the laser leads to a broadening of the line which can be described via an undamped oscillator with the spectral intensity profile $I(\omega)$:

$$I(\omega) = C\frac{\sin^2(\omega - \omega_0)T/2}{(\omega - \omega_0)^2} \tag{6.11}$$

The field amplitude E of a laser mode is given by $E = E_0 \cos \omega t$. With the relation that the amplitude is proportional to the oscillator and the damping time is still the smallest, the FWHM can be obtained for a Gaussian beam profile.

$$\mathrm{FWHM}_{LP} \approx \frac{2.4\nu}{w} \tag{6.12}$$

w is the beam waist of the Gaussian profile and ν the molecular velocity.

6.6 Homogeneous and Inhomogeneous Line Broadening

It subdivides the broadening effects into two parts and defines them. If every molecule in the ensemble affected equally for example causing a transition, it's homogeneous broadened. The spectrum of one molecule would still be the same and it leads to a normalized Lorentzian profile [46]. Collisional broadening, laser profile broadening and lifetime broadening are homogeneous effects.

Inhomogeneous broadening results from molecules with different resonant frequencies. This occurs because they are in slightly different local environments within a liquid or gas, or they have different velocities. This is the case by Doppler Broadening. The

observed broadening of the spectrum arises from a superposition of a large number of slightly different spectra. Also, the collision of two molecules with different velocities v_{z2} and v_{z2} can change a subgroup of a molecule. For example from subgroup v_z to $v_{z1} + v_{z2}$ the resulting frequency shifts from $\omega \to \omega + kv_{z2}$.

This negligible broadening has to be named because of the upcoming saturation spectroscopy experiment. If the interaction time t_c is smaller then the mean time of collisions T_t the subgroups mix and a broadening is associated with each subgroup [46].

6.7 Voigt Profile

To characterize a frequency distribution in molecular spectroscopy, where both a Gaussian and a Lorentzian broadening mechanism occur, the Voigt function can be used. It is a convolution of a Lorentzian distribution and a Gaussian distribution. It involves Doppler broadening γ_D and the lifetime broadening γ_τ. In the experimental setup $\gamma_D \gg \gamma_{coll}$ and γ_{coll} can be neglected. The FWHM of the numeric Voigt function is associated by Gaussian and Lorentzian FWHM [47]:

$$\mathrm{FWHM}_V \approx 0.5346\,\mathrm{FWHM}_D + \sqrt{0.2166\,\mathrm{FWHM}_D^2 + \mathrm{FWHM}_L^2} \tag{6.13}$$

6.8 Power Broadening

As the saturation spectroscopy is mentioned, high intensities decrease the population in absorbing levels. It's because of the larger pumping rate which leads to additional line broadening. These effects can also be divided into homogeneous and inhomogeneous.

6.8.1 Saturated Absorption Coefficient

Investigate a two level system, the level populations N_1 and N_2 can be described via transition probability P for a transition of photons or also called pumping rate and relaxation probability R_1 and R_2. When $P = 0$, the level populations are $N_{10} = \frac{R_2}{R_1+R_2}N$ and $N_{20} = \frac{R_1}{R_1+R_2}N$. This leads to the equation:

$$\Delta N = \frac{\Delta N_0}{1 + 2P/(R_1 + R_2)} = \frac{\Delta N_0}{1 + S} \quad \text{with} \quad \Delta N_0 = N_{10} - N_{20} \tag{6.14}$$

with S as the saturation parameter. The equation shows that with higher R the term goes to zero, which concludes to a transparent medium instead of an absorption. The saturation parameter S is defined as the ratio between pumping rate and the average relaxation rate $\bar{R} = (R_1 + R_2)/2$.

The Lambert-Beer-Law described an extinction coefficient for light transmission through a medium, a saturated absorption coefficient $\alpha(\omega) = \delta_{12}\Delta N$ is used to describe the absorption profile and homogeneously broaden effects [48]. Together with eq. 6.14 it's:

$$\alpha = \frac{\alpha_0}{1 + S} \tag{6.15}$$

where α_0 is the unsaturated absorption coefficient without pumping. This broadening effect is a Lorentzian with $\gamma_S = \gamma\sqrt{1 + S_0}$ as halfwidth. Together with the spectral saturation parameter S_ω, the coefficient is defined as:

$$\alpha_s(\omega) = \alpha_0(\omega_0)\frac{(\gamma/2)^2}{(\omega - \omega_0)^2 + (\gamma_s/2)^2} = \frac{\alpha_0(\omega)}{1 + S_\omega} \tag{6.16}$$

A decrease of the coefficient comes from increasing the denominator. With a maximum when $\omega - \omega_0 \to 1$.

6.8.2 Spectral Hole Burning

These saturation effects take part when an inhomogenous broadening like Doppler is affecting the line profile. The easiest way to understand these effects is through a measurement. Two laser beams, one pump beam with enough power to saturate a transition, and one probe beam are aligned through a gas cell.

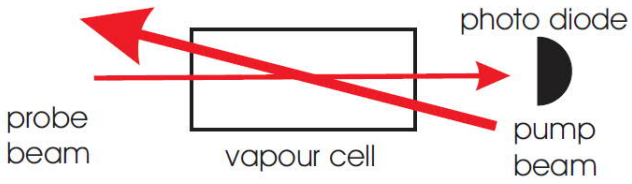

FIGURE 6.1: Beam arrangement for saturation spectroscopy.
Figure reprinted from [12]

The probability if a photon is absorbed depends on the velocity v_z. This movement also leads to a Doppler shift of the light frequency ω with $\omega' = \omega - \nu_Z * k$. Only the molecules get contributed who are in the range of $\omega' = \omega_o \pm \gamma$. Due to saturation the population densities of a two-level system N_1 and N_2 changes, such that N_1 decreases and N_2 increases. These results in peaks or holes in the velocity distribution which are named after the discoverer Bennet [12].

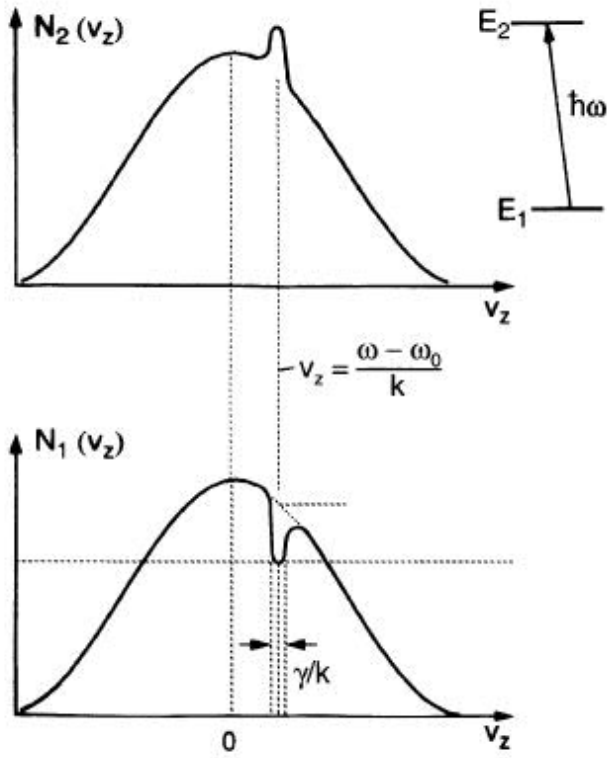

FIGURE 6.2: The upper graphic shows a Bennet peak in the upper state population density N_2 plotted as function of the velocity. The lower graphic shows a Bennet hole in the lower state population density N_1 plotted as function of the velocity.
Figure reprinted from [13]

The hole as a width of $\gamma_s = \gamma(1+S_0)^{\frac{1}{2}}$ and the depth is described by:

$$\Delta\alpha(\omega') = \frac{S_0}{\sqrt{1+S_0}(1+\sqrt{1+S_0})} \tag{6.17}$$

Since every molecule with the right velocity distribution is involved in the absorption, the absorption coefficient $\alpha(\omega)$ gives a Voigt profile. The coefficient is defined as:

$$\alpha(\omega) = \frac{\alpha^0(\omega)}{\sqrt{1+S_0}} \tag{6.18}$$

with $\alpha^0(\omega)$ as the unsaturated absorption coefficient. The exact derivation can be seen in [13]. Every laser, independent of it's frequency can results in a Bennet hole. The reduction of the absorption coefficient is the same for every frequency by the factor $(1+S_0)^(1/2)$. So the absorption itself can't explain the minimum but the inclusion of an extra laser beam, the probe beam, makes the Bennet hole visible in a spectrum. This effect only takes part when the laser frequency is not exactly equal to the resonance frequency of the molecules. When two beams counter propagate with the same frequency it results in a Lamb-dip.

6.8.3 Lamb-Dip

The two counter propagating waves with wave vector $\vec{k_1}$ and $\vec{k_2}$ result in two Bennett holes with the velocity components $v_z = +$ and $v_z = -$ in the population distribution. At $\omega = \omega_0$ these overlap and generate a so-called Lamp-dip. It's a dip at the line center with a Lorentzian profile. In an absorption spectrum, it is duo the saturation of the transition at the center of a single line and the process is Doppler-free [49]. The absorption coefficient is defined for a molecule in a standing wave as:

$$\alpha_s(\omega) = \alpha^0(\omega)[1 - \frac{S_0}{2}(1 + \frac{(\gamma_s/2)^2}{(\omega-\omega_0)^2 + (\gamma_s/2)^2})] \tag{6.19}$$

with $\gamma_s = \gamma\sqrt{1+S_0}$ and $S_0 = S_0(I, \omega_0)$.

The depth of a Lamp-dip is $S_0 = B_{i\vec{k}}I/(c\gamma_s)$ with c as velocity of light and $B_{i\vec{k}}$ as transition probability. Because the power stimulated in a Lamb-dip falls within about a

natural width of atoms' Doppler-shifted frequency, the number of atoms stimulated to emit at the line center can decrease by a factor of two [50].

Chapter 7

Optical Spectroscopy of the $b^3\Sigma^+, v = 5//A^1\Pi, v = 6$ Perturbed Complex of AlF

In this chapter, spectroscopic studies are carried out on the lowest rotational levels of aluminum monofluoride, using the PDL and the PDA. There will be a closer look at the $b^3\Sigma^+, v = 5//A^1\Pi, v = 6$ perturbed complex.

7.1 Experimental Data on the Rotational Structure of AlF

Because of the diagonal Franck Condon matrix between X, a, and b states, the $\Delta v = 0$ transitions are much stronger than all other transitions. Therefore all measured spectra in the upcoming chapters are $\Delta v = 0$.

7.1.1 General Selection Rules

To measure a valid diatomic spectrum, selection rules for the individual quantum numbers have to be taken into account. For the electronic states of AlF, X, a, and b the rules are:

$$\Delta\Lambda = 0, \pm 1 \tag{7.1}$$

and for the total spin S

$$\Delta S = 0 \tag{7.2}$$

The ΔS-rule explains that transitions between triplet states are allowed and transition from singlet to triplet states are forbidden. Under consideration of Hund's coupling case two additional selection rules can be derived:

$$\Delta J = 0, \pm 1 \quad \text{with} \quad J = 0 \nleftrightarrow J = 0 \tag{7.3}$$

and the parity rule:

$$+ \nleftrightarrow +, - \nleftrightarrow -, + \leftrightarrow - \tag{7.4}$$

Eq. 7.4 shows that only transitions between states of opposite parity are allowed. But an electrical field, produced from a laser or a different external influence, can mix the states with different parities. This so-called parity mixing allows transitions between states of the same parity.

The data from the (1+1')-REMPI, obtained with the PDL via the $b^3\Sigma^+$ state, gives an overview spectrum of the lowest vibrational levels of the b-state, which can be seen in Fig. 7.1. Transitions with $\Delta J = -1, 0, 1$ are designated as $P-, Q-$ and R-lines and are separated by the factor $2B$, with B as the rotational constant in wavenumber, to each other.

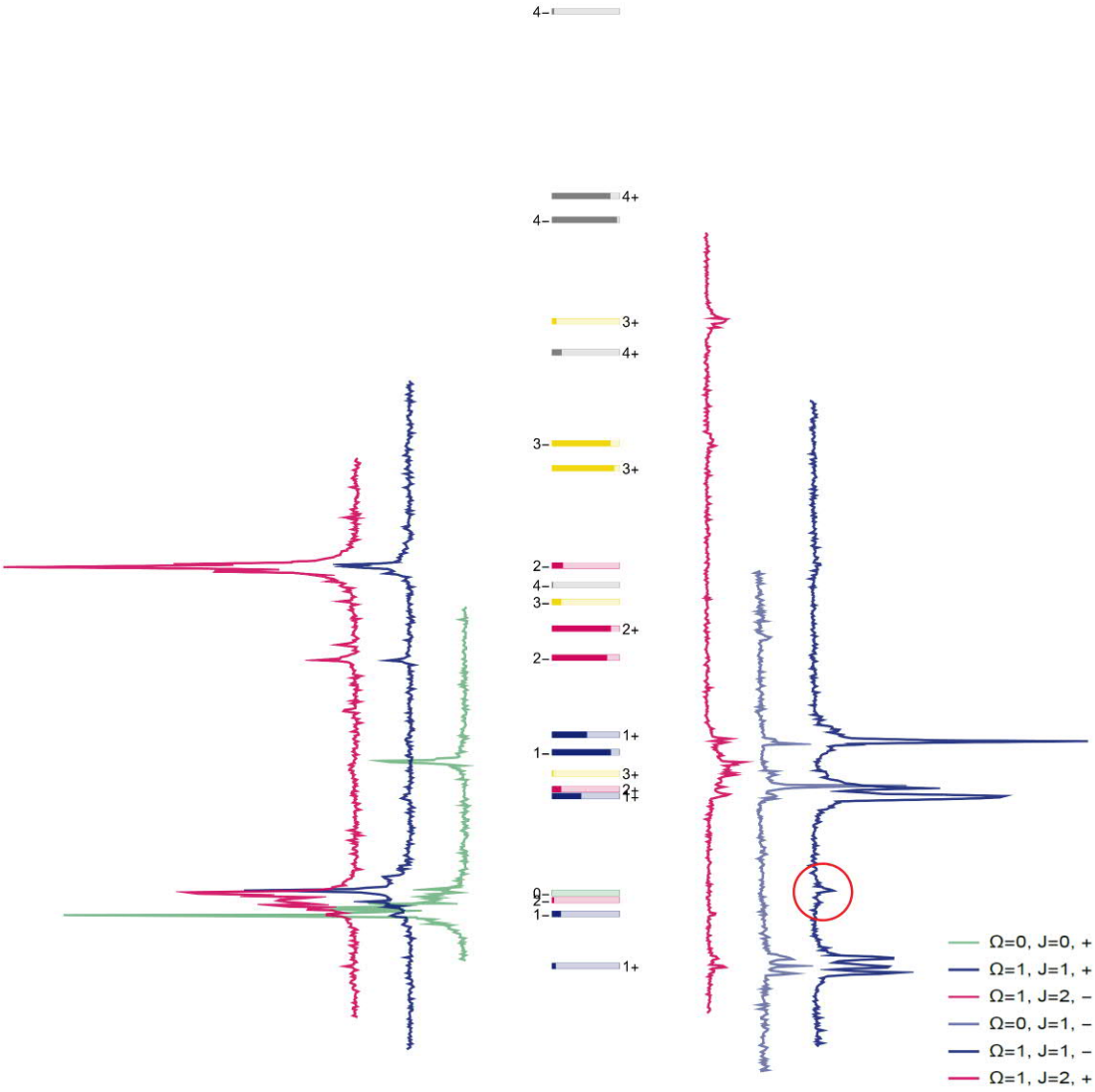

FIGURE 7.1: Overview of the rotational strucutre of AlF.

The $a \leftarrow X$ laser excites AlF molecules from the X ground state to an a triplet state. It is possible through the spin-orbit coupling of the a and the A state and the high energy of the laser. Since only $\Omega = 1$ can perform a spin-orbit coupling, the transitions to the $a^3\Pi$ state are the strongest. On the left side are all negative b state transitions which are excited from a positive a state and the other way around on the right side. An exception is the red circled peak, which comes from parity mixing created from a disturbing electrical field. The ΔJ selection rule can be confirmed on every spectrum. The bar in the middle of Fig. 7.1 describes the singlet $S = 0$ and triplet $S = 1$ character of the transitions. If the filling of the bar gets higher, the transitions have more singlet character. That allowed transition need a lot less energy and can be seen in the red

$J = 2, +$ spectra. Both $J = 3, N = 1, +$ peaks can be found in the red spectra as well. The $J = 3, N = 0, +$ isn't visible.

7.2 Experimental Data of the Rotational Structure with a Pulsed Dye Amplified RDL

To better resolve the structure of the $b^3\Sigma^+, v = 5//A^1\Pi, v = 6$ perturbed complex, a higher resolution is acquired. The PDA is used to obtain the $\Omega = 1$ spectra of the a state and the $N = 0, 1, 2, 3$ transitions of the b state. The result gives higher accuracy on the wavenumbers for all transitions and allows a future hyperfine structure measurement. Since showing every spectrum will be too much, there will be a closer look at the $b^3\Sigma^+, v = 5//A^1\Pi, v = 6 \leftarrow a^3\Pi, v = 5$.

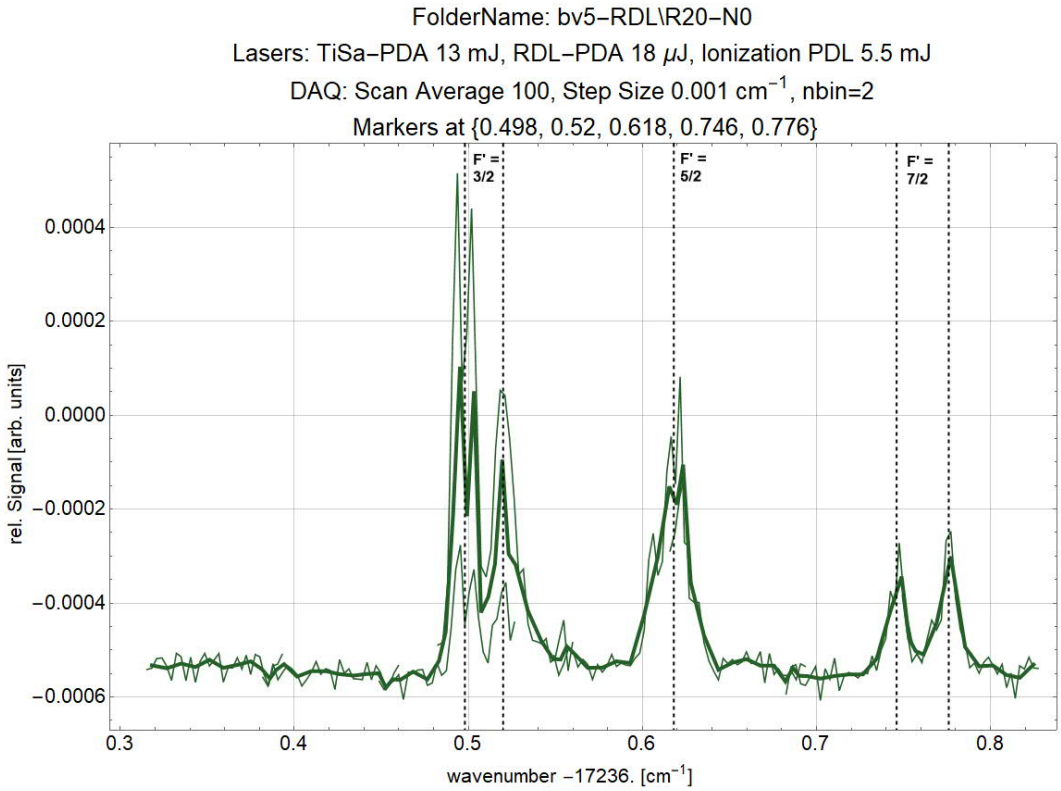

FIGURE 7.2: Experimental Data of the $b, v = 5R_2(0), J = 1$ transition measured with the PDA.

To describe the spectra, the intermediate quantum number F' is introduced. F' describes the coupling of J with the nuclear spin of aluminium $I_{Al} = 5/2$.

$$F' = J + I_{Al}, ..., |J - I_{Al}| \tag{7.5}$$

The $b^3\Sigma^+$ $N = 0$,$J = 1$ level splits into:

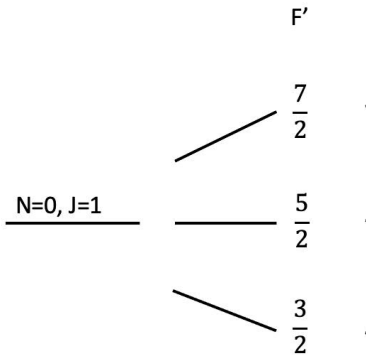

FIGURE 7.3: Overview of the F' splitting of AlF.

The experimental data, Fig. 7.2, is obtained with 5.5 mJ, a scan average of 100 and a step size of 3 MHz. Every peak is measured multiple times, declaring the transitions to the exact frequencies and their depending F'. The data is acquired with (1+1')-REMPI. The results show that (1+1')-REMPI works with the PDL and the PDA as excitation lasers for the $b \leftarrow a$ transition of AlF. The recorded spectra are composed of 2.5 GHz scans of the PDA. Since the spectra show even more peaks the hyperfine structure of AlF can be investigated. Therefore the RDL is used since its linewidth is narrower than a laser pulse of the PDA.

Chapter 8

Investigation of the Hyperfine Structure of AlF and Lamb-Dip Measurements

In this chapter, the hyperfine spectroscopic studies are carried out in the lowest rotational levels of the $v = 5$ level in the $a^3\Pi_1$ state of AlF. The values of the hyperfine parameters and their change from $v = 0$ to $v = 5$ are investigated. Also, a closer look at the perturbed region described in the previous chapter is realized by using the RDL as a continuous wave excitation laser. Finally, the stability of the RDL is tested by measuring a Lamb-dip with saturated spectroscopy.

8.1 Hyperfine Structure of AlF

Nuclear spin coupling is the foundation for a hyperfine structure. The quantum number F is introduced to label the later coupling of F' with the nuclear spin of fluorine $I_F = 1/2$:

$$F = F' + I_F, ..., |F' - I_F| \tag{8.1}$$

The selection rule $\Delta F = \pm 1$ is inviolable compared to the other selection rules and always applies.

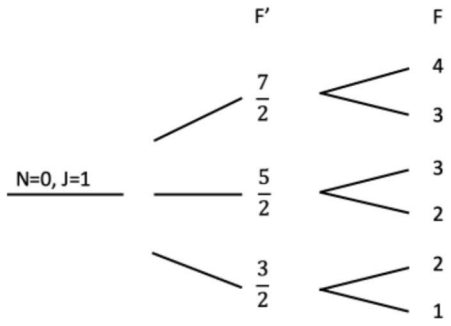

FIGURE 8.1: Overview of the F splitting of Alf.

An overview of the hyperfine structure in the $a^3\Pi$ state and $A^1\Pi$ state can be found in [15]. The hyperfine structure of $b^3\Sigma^+$ state can be seen in [51]. An overview of the F-levels of the $b^3\Sigma^+, v = 5//A^1\Pi, v = 6$ perturbed complex is shown in Fig. 8.2.

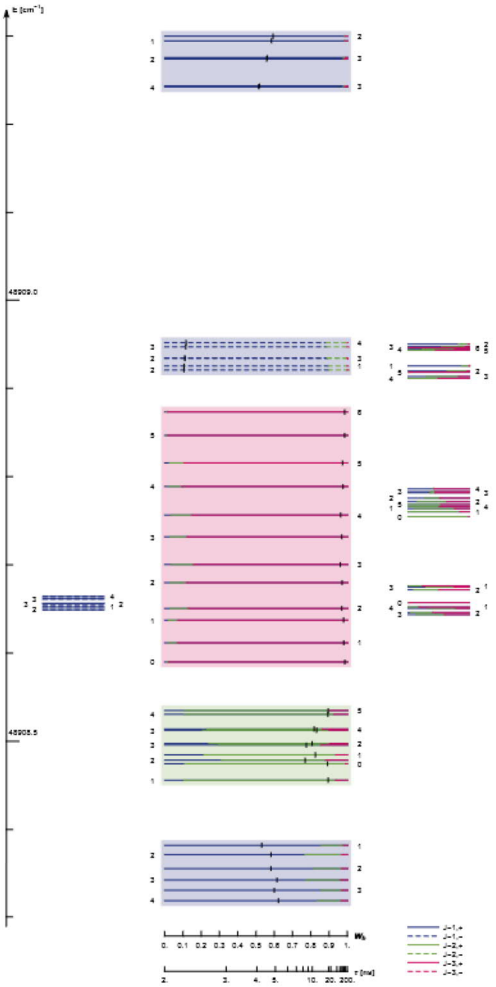

FIGURE 8.2: Energy level scheme of the hyperfine structure of Alf.

The coloring is labeled to the different J-levels and the numbers on the side labeling the F-levels. The black bars show the lifetime τ of the states and the weight of the b-character W_b.

8.2 Experimental Data of the Hyperfine Structure of AlF

The results of the fine structure measurements are used as a template for the following measurements. The resolution spectra are obtained using LIF, Fig. 4.4. The RDL is reduced to 5 mW, to avoid power broadening. Every peak is measured multiple times which allows to deduce the SBS-shift. There will be a look at the high-resolution LIF spectra of the $J = 1, N = 0$ transitions and from the $J = 0$ in the a state to $J = 0, J = 1$ of $N = 1$, see Fig. 8.3. These determine the hyperfine structure of $b^3\Sigma^+, v = 5$ state, and a comparison to the PDA spectra Fig. 7.2 shows, that the resolutions allow the labeling of the independent F-levels.

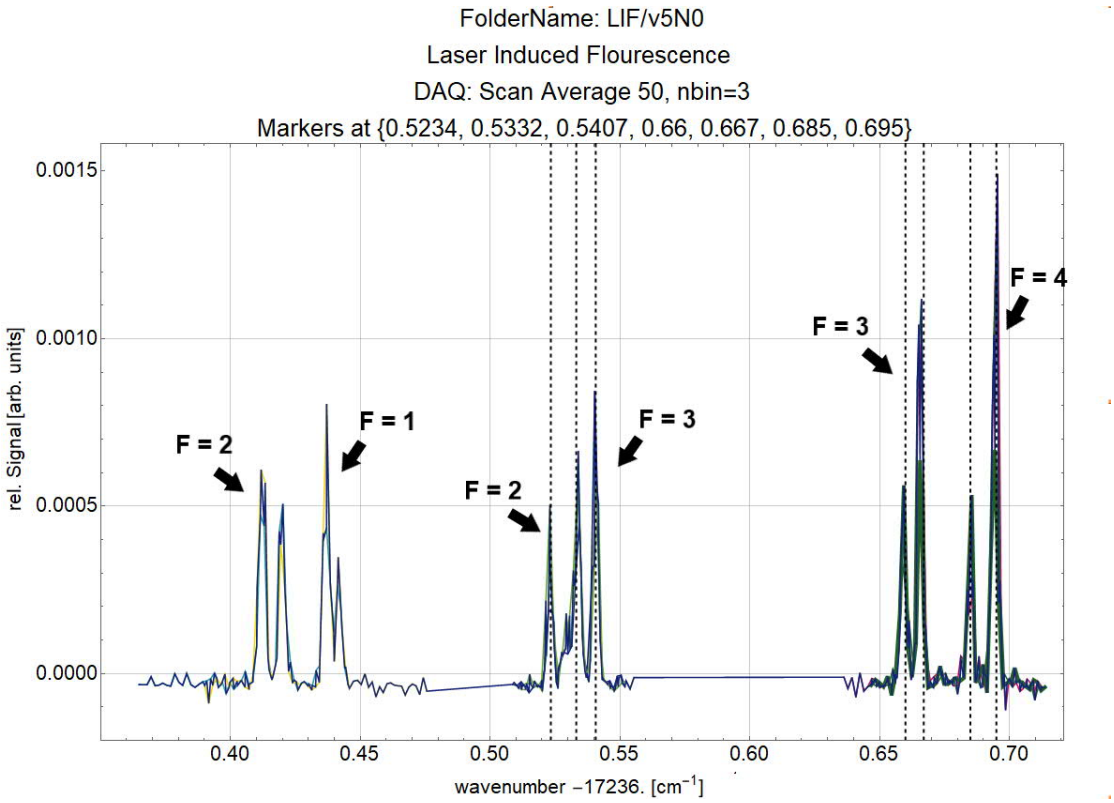

FIGURE 8.3: RDL excited LIF spectra along the R2(0) line: $b^3\Sigma^+, v = 5 \leftarrow a^3\Pi, \omega = 1, v = 5$.

8.2.1 Comparison of the Resolution of the PDL, PDA and RDL Scans

The active stabilization together with the new alignments of the RDL, allowed using the RDL as a permanent tool for spectroscopy. Since the linewidth of a cw dye laser is smaller than the pulsed laser systems, the investigation of the hyperfine structure of AlF without using microwave transitions became possible. Fig. 8.4 shows the exact comparison of the resolution using the PDL (green), the PDA (pink), and the RDL (blue) as a LIF measurement. The PDL scans with a resolution towards the splitting of the quantum number F'. It has to be mentioned that the power of the PDL is around $15\,\mu$J, otherwise, the power broadening reduces the spectra to only one peak. These measurements are necessary to find the line positions of AlF. The hyperfine structure can be resolved when using the PDA but only the cw RDL with its even smaller linewidth allows to resolve the hyperfine structure such that an exact labeling of the transition up to several MHz is possible.

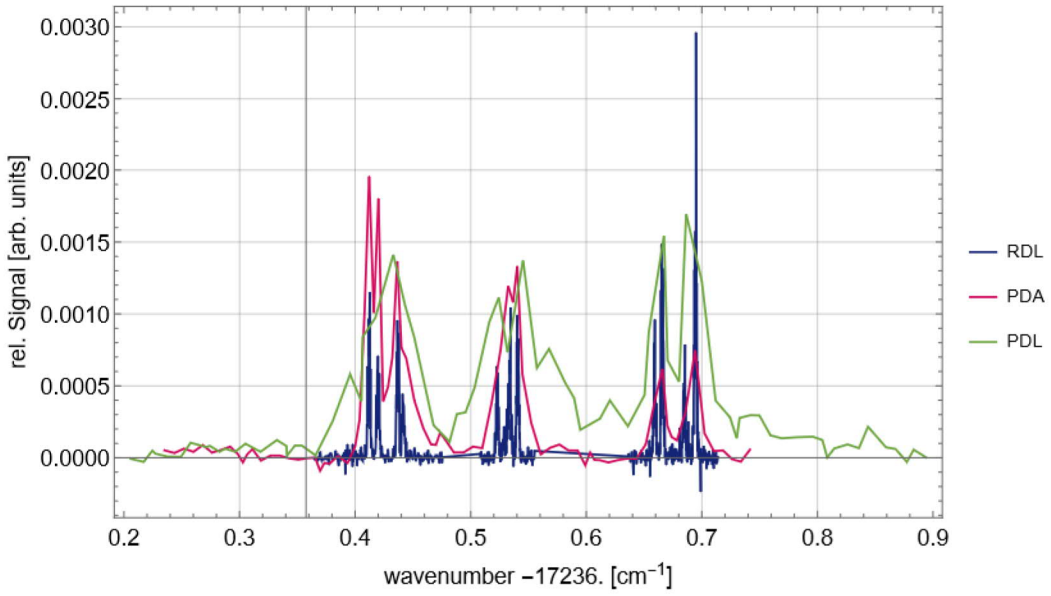

FIGURE 8.4: Comparison of the spectral resolution obtained the different laser systems of the PDL (green), the PDA (pink), and the RDL (blue).

8.2.2 SBS-Shift Validation through the High Resolution Spectra

The acquired high-resolution LIF spectra using the cw RDL also enable the determination of SBS-shift, since the absorption spectrum from 8.4 were measured with the PDA, which includes the SBS-shift. The same spectrum obtained with LIF, recording the $b^3\Sigma^+, v = 5 \rightarrow a^3\Pi, v'$ emission with the RDL, has no frequency shift. To find

the line positions the result of the previous SBS-shift measurements ($0.085\,\mathrm{cm}^{-1}$) were used. The wavemeter and the digitizer card are the same, resulting in uncertainty of 1 MHz. The SBS-shift is obtained through an optical overlap which leads to a value of $0.083\,\mathrm{cm}^{-1} \pm 0.001\,\mathrm{cm}^{-1}$ or $2.49\,\mathrm{GHz} \pm 30\,\mathrm{MHz}$. Thus, this procedure not only offers a new measurement method, it also validates the values of section 3.1.1 with an even lower error bar.

8.2.3 Comparison of the calculated and measured Frequency Dependency of the SBS-Shift

At this point there is strong evidence that the SBS-shift shows a dependency on the laser light frequency ν_L. In the investigations the observed general behaviour of the SBS-shift increases as a function of increasing laser frequency. The shorter the wavelength gets the larger the SBS-shift becomes. According to the specifications and the manual of the manufacturer of the PDA system and its SBS-cells, Sirah Ltd., the SBS-shift should be constant [52]. Since the manufacturer did not tell what particular liquid has been used in the SBS-cell of the PDA, a calculation of the SBS-shift using eq. 3.2 and several different liquids given in [31], where the SBS-shift for water is listed with 5.91 GHz at a wavelength of 694 nm, is performed.

In the optical setup the scattering angle is $\theta = 180°$. Thus the SBS-shift is calculated for water using $v_s = 1418\,\frac{\mathrm{m}}{\mathrm{s}}$ for the speed of sound and $n = 1.33$ as refractive index at the wavelengths of 580 nm and 733 nm. As an exact dependency of the SBS shift is a function of the frequency is difficult to predict, the calculation gives the ratio of 1.28 for the experimentally determined SBS shifts at 580 nm than at 733 nm. This ratio corresponds to the scaling factor by how much the SBS-shift increases with increasing laser frequency. Since the calculated values for the SBS-shift of water at two different wavelengths correspond quite well, calculation of the ratio for other solvents such as Benzene ($v_s = 1298\,\frac{\mathrm{m}}{\mathrm{s}}$, $n = 1.50$), Ethanol ($v_s = 1159\,\frac{\mathrm{m}}{\mathrm{s}}$, $n = 1.36$) and Aceton ($v_s = 1170\,\frac{\mathrm{m}}{\mathrm{s}}$, $n = 1.36$) are carried out. Tab. 8.1 shows the results where it must be concluded that no matter what liquid Sirah Ltd is using as SBS medium, given the correct values of the speed of sound and the refractive index, the SBS-shift will be the same independent of the liquid. Moreover, this also proves that the observed frequency dependence of the SBS-shift is evident.

TABLE 8.1: Comparison of the experimental and calculated SBS-shift.

Wavelength	580 nm	733 nm	Ratio of the frequency change
SBS-shift (meas.)	2.49 GHz	1.94 GHz	1.28
SBS-shift of Water (calc.)	6.79 GHz	5.37 GHz	1.26
SBS-shift of Ethanol (calc.)	5.43 GHz	4.30 GHz	1.26
SBS-shift of Benzene (calc.)	6.71 GHz	5.31 GHz	1.26
SBS-shift of Aceton (calc.)	5.48 GHz	4.34 GHz	1.26

In the following, a qualitative idea is described that might explain why the SBS process shows a laser frequency dependency to $1/\lambda$. First of all, the energy has to be conserved in the SBS process. The energy of the incoming photon is partly converted into the creation of phonons that cause the sound wave and thereby the periodic density modulations in the SBS medium. Therefore the energy of the outgoing photon is smaller, and thus the wavelength of the outgoing (back-reflected) wave is always longer than that of the incoming one. The back-scattering takes place on a periodic structure that is set up by the incoming laser wavelength as given in eq. 3.1 divided by the refractive index. Therefore the energy of the created phonon proportionally increases with an increase of the laser which would explain why the frequency dependence of the SBS-shift.

8.3 Lamb-Dip Measurements with LIF

To obtain the lifetime of a transition without Doppler broadening, saturated spectroscopy has to be performed. This will also be the final test of the stability and scanning of the RDL.

8.3.1 Lamb-Dip Experiment on AlF

The Lamb-dip measurements were performed on the transition from the $F = 3, J = 0$, positive parity, e-level in the $a^3\Pi_0, v = 5$ state to the $F = 4, J = 1, N = 1$, negative parity, e-level in the $b3\Sigma^+, v = 5$ state around $17286.316\,\mathrm{cm}^{-1}$. The calculated peak absorption cross-section σ_0 for this particular transition is equal to $\sigma_0 = 7.6 \cdot 10^{-12}\,\mathrm{cm}^2$. The lifetime of this perturbed state is obtained from the measured lifetimes τ_a of the $A^1\Sigma, v = 6$ state 1.90 ns [15] and τ_b of the $b^3\Sigma^+, v = 5$ state 190 ns [53].

In the experiment, the setup from Fig. 4.4 is extended. The RDL beam is expanded with a telescope and aligned through a slit with a 0.4 x 1.0 cm^2 area. The laser is set at 17286.346 cm^{-1} and 3.5 mW intensity (after the slit) which leads to an intensity $I = 2.5 \cdot 1016$ photons per cm^2 and per second. The interaction time T is well defined by the 4 mm long interaction region, which the molecules pass with a speed of about 800 m/s to be T=5 μs. The RDL is back-reflected with a mirror instead of divided into a probe and pump beam, to excite the molecular beam. The time-integrated intensity by the incoming beam can be seen in Fig. 8.5.

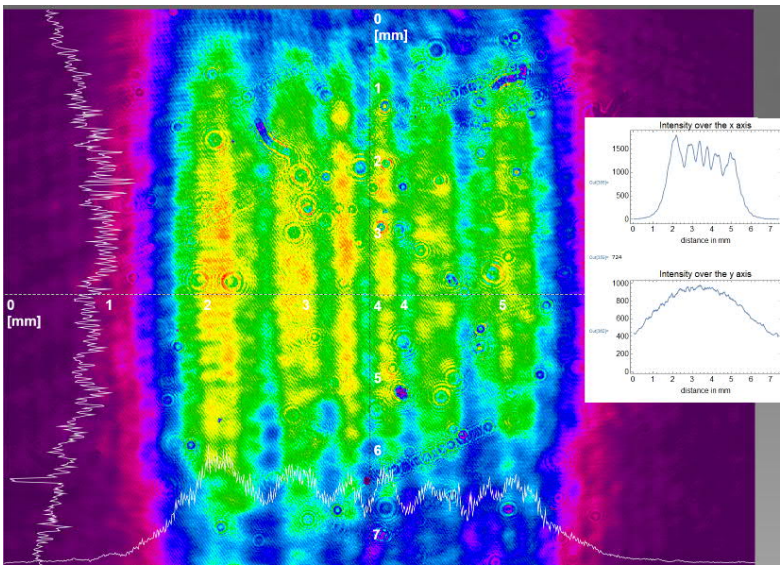

FIGURE 8.5: Intensity profile of the RDL after the slit, measured with a beam camera.

It is assumed that the back-reflected beam has the same intensity as the incoming beam ($R \geq 0.99$). The UV fluorescence is detected with a photomultiplier tube as a function of the frequency of the RDL. Since the beam camera can't obtain the complete profile with one picture because of its chip size (7.38 x 7.38 mm), several pictures are taken and added up. A three-dimensional profile of the beam can be seen in Fig. 8.6.

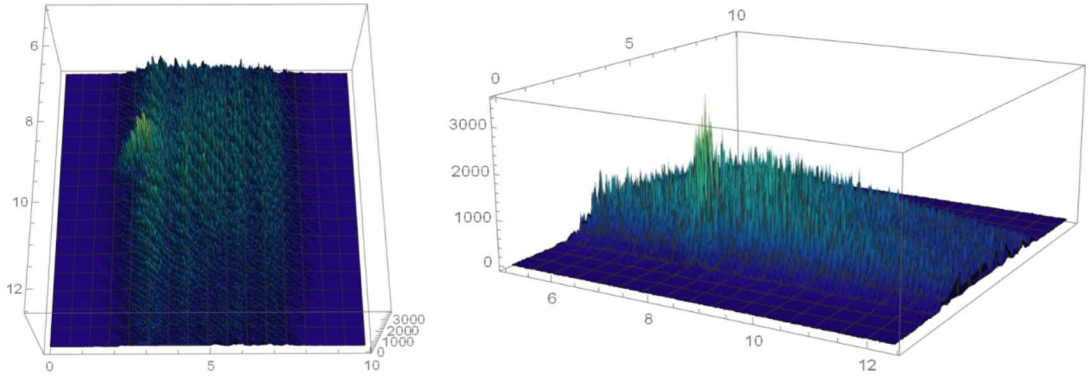

FIGURE 8.6: Three dimensional intensity profile of the RDL after the slit, measured with a beam camera.

The peak which can be seen in Fig. 8.6 is duo a chip defect on the beam camera and can therefore be neglected. In the molecular beam, there is inhomogeneous and homogeneous broadening so the absorption profile is described with a Voigt profile. When Doppler broadening is the largest broadening factor the Voigt profile scales with $1/\sqrt{1+S_0}$. The Gaussian contribution due to the residual Doppler broadening is about 67 MHz with a Lorentzian Lamb-dip at the center. The measured Lamb-dip can be seen in Fig. 8.7.

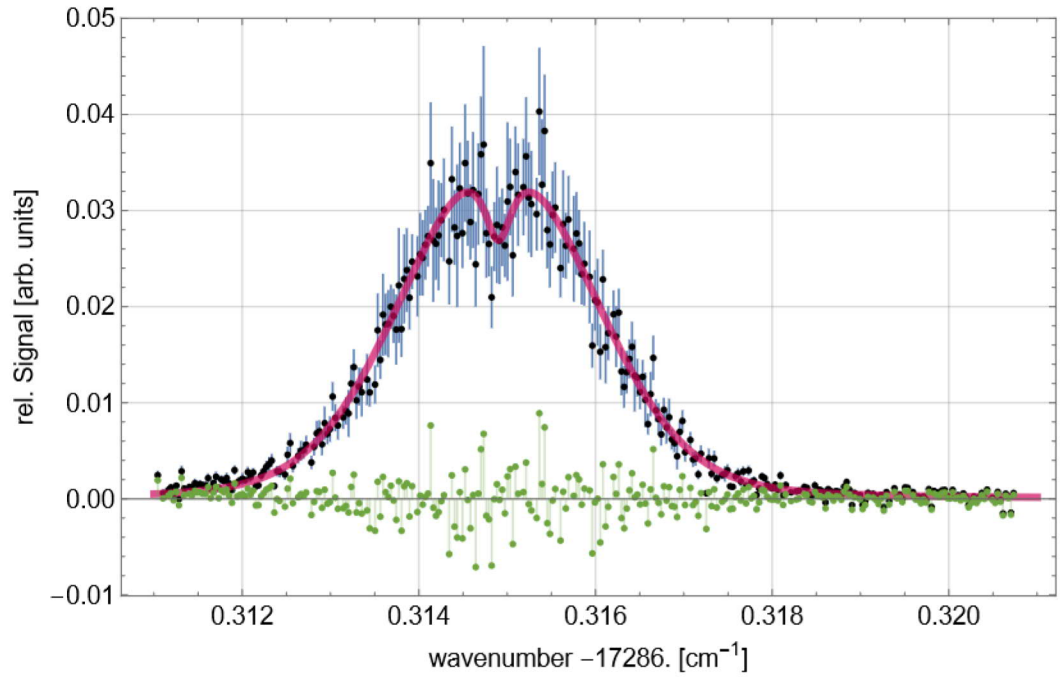

FIGURE 8.7: Lamb-dip measurement on the single transition line at 17286.314 cm^{-1}. Blue is the raw data with error bars in black. Pink is the Lamb-Fit which consists of a Voigt profile with a Lorentzian dip at the center. The residuals of the data and the Voigt profile are plotted in green.

Because of the composition of multiple scans, the resolution is even below the step size. With a step size of 3 MHz, the fluctuation of 1.5 MHz, leads to more data points around the peak. The Lamb-dip has a depth of $D(\nu_0) = 0.25$ and a width of $W(\nu_0) = 12\,\text{MHz}$. The uncertainty in this experimental value is a rough estimate, based on the error bar in the value of $D(\nu_0)$ and the homogeneity of the laser intensity distribution over the rectangular area. The lifetime is experimentally determined to $\tau \approx 17.4\,\text{ns}$.

The LIF experiment in a Lamb-dip setup also demonstrates that a line with a width of only 12 MHz can be measured by the RDL. Fig. 8.8 shows a resulting Lorentz from the Lamb-Dip measurement at $17286.314\,\text{cm}^{-1}$ plotted in MHz. Therefore a Voigt profile is subtracted from the data and the data is fitted to a Lorentz. The new frequency stabilization and alignment enabled frequency scans of around 1.5 MHz, which is only limited by the jitter of the RDL. The reproducible recording of molecular spectra demonstrates the frequency tune-ability and scanning of the RDL.

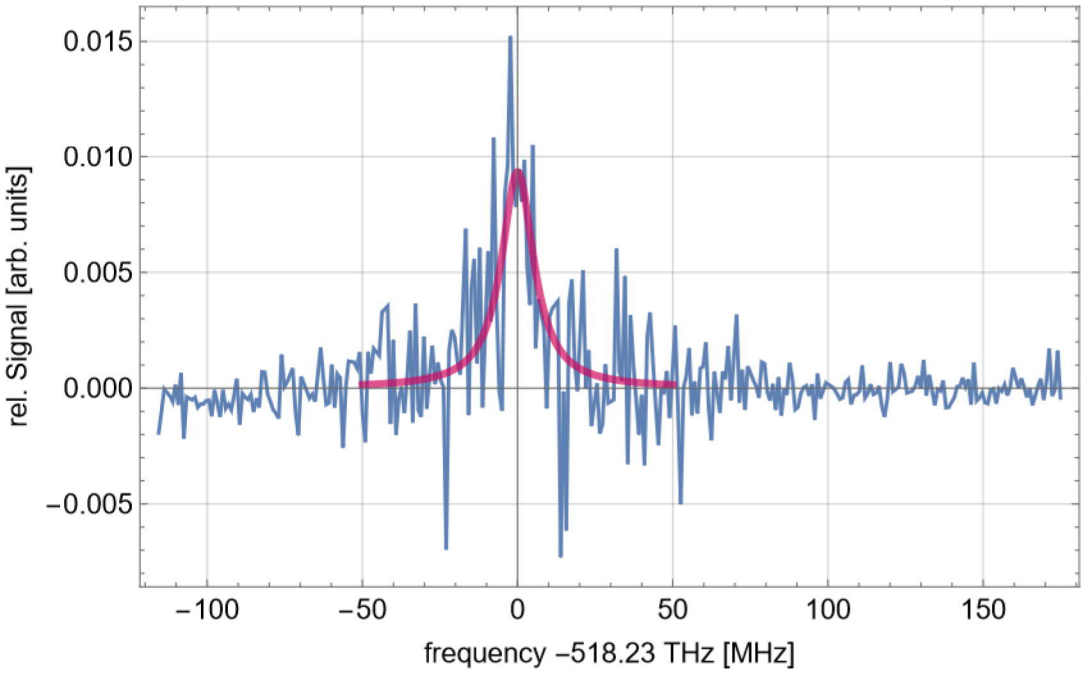

FIGURE 8.8: Resulting Lorentz from the Lamb-Dip measurement at $17286.314\,\text{cm}^{-1}$ plotted in MHz. Blue shows the data subtracted by the Voigt profile. Pink is a Lorentz-Fit.

Chapter 9

Summary and Outlook

The goal of this thesis is the characterization and frequency stabilization of a continuous wave ring dye laser and the experimental usage for molecular spectroscopy. The beam divergence Θ=0.75 mm were determined for the first time with the new components. The new alignment enabled a power improvement of around 20 % to 1000 mW at 578 nm.

The comparison of the frequency stabilization shows an improvement in the controlling and scanning of the RDL. It enabled mode-hop free scans with a scan range of 10 GHz and high-resolution measurements, limited by a jitter of 1.5 MHz.

The PDA could be seeded with the RDL and the laser pulses were used for spectroscopy on the molecular beam machine. SBS-shift measurements showed new results for a factory-given frequency shift. With high-resolutions scans on AlF and iodine absorption measurements, a SBS-shift of around 2.49 GHz could be obtained. This result was confirmed in multiple high-resolution scans and other methods showed comparable results with the highest deviation of 100 MHz. The data is handed over to Sirah Lasertechnik, where further procedures are now discussed.

Since the diatomic molecule AlF is the chosen candidate for laser cooling, the investigation with the RDL brought new information. The (1+1')-REMPI measurements on AlF, showed hyperfine resolution spectra without microwave transitions. The obtained information about the location of the spectra peaks could be used to calculate all F states of Alf. Afterward, the LIF-spectra enabled an assignment of all levels and exact frequencies in the order of MHz.

A final stability test is fulfilled by measuring a Lamb-Dip of a 12 MHz on a single transition line of AlF. This highlights the frequency tune-ability and scanning of the RDL and remarks the laser as an inherent part of spectroscopy.

The next improvement for the frequency stabilization of the RDL will be to lock the laser to a narrow line iodine transition with modulation transfer spectroscopy. For this purpose, the laser frequency is stabilized to resonance by detecting a fluctuation of the frequency instead of changing the free spectral range of the Fabry-Perot interferometer. This could enable a linewidth and stability in the kHz region.

Bibliography

[1] W.G. Nagourney. *Quantum Electronics for Atomic Physics and Telecommunication*. Oxford graduate texts. Oxford University Press, 2014. ISBN 9780199665488. URL https://books.google.de/books?id=YDOTAwAAQBAJ.

[2] Jarag K.J. Shankarling G.S. Laser dyes. *Resonance*, 15, 11 2010. doi: 10.1007/s12045-010-0090-9.

[3] H.J. Eichler and J. Eichler. *Laser: Bauformen, Strahlführung, Anwendungen*. Springer Berlin Heidelberg, 2015. ISBN 9783642414381. URL https://books.google.de/books?id=4n7DCgAAQBAJ.

[4] Sirah Lasertechnik. Dye circulator. 2021. URL https://www.sirah.com/accessories/dyes-for-matisse-2-d-series__trashed/circulators/.

[5] Giorgio Bardizza. *Setup of a narrow linewidth UV/VIS laser system for high-resolution spectroscopy of cold large molecules*. PhD thesis, Master Thesis, 2003/2004, Univcsrit'a statalc dcgli studi di Milano.

[6] *Operator's Manual, The Coherent 889-21 Dye Ring Laser*.

[7] Praktikum he-ne laser. 2020. URL https://www.tu-chemnitz.de/physik/FPRAK/F-Praktikum/Versuche_alt/HeNe-Laser20MEOS.pdf.

[8] Sirah Lasertechnik. *Sirah Pulsed Amplifier*. URL https://www.photonicsolutions.co.uk/upfiles/PulsedAmplifierDatasheetLG19Apr18.pdf.

[9] Matisse 2 tunable ring laser. URL https://www.spectra-physics.com/f/matisse-2-tunable-ring-laser.

[10] Simon Hofsäss, Maximilian Doppelbauer, Sid Wright, Sebastian Kray, Boris Sartakov, Jesús Pérez-Ríos, Gerard Meijer, and Stefan Truppe. Optical cycling of alf molecules, in press.

[11] R F Barrow, I Kopp, and C Malmberg. The electronic spectrum of gaseous AlF. *Physica Scripta*, 10(1-2):86–102, jul 1974. doi: 10.1088/0031-8949/10/1-2/008. URL https://doi.org/10.1088%2F0031-8949%2F10%2F1-2%2F008.

[12] Thomas Rieger and Thomas Volz. Doppler free saturation spectroscopy. doi: 10.1103/PhysRev.79.549. URL https://www.mpq.mpg.de/4992695/saturation_spectroscopy.pdf.

[13] W. Demtröder and M. Roach. *Laser Spectroscopy: Basic Concepts and Instrumentation*. Advanced Texts in Physics. Springer Berlin Heidelberg, 2013. ISBN 9783662051559. URL https://books.google.de/books?id=lfTxCAAAQBAJ.

[14] Max Doppelbauer Stefan Truppe and Simon Hofsäss. Truppe's cold molecule lab. 2020. URL https://www.fhi.mpg.de/254299/Research.

[15] S. Truppe, S. Marx, S. Kray, M. Doppelbauer, S. Hofsäss, H. C. Schewe, N. Walter, J. Pérez-Ríos, B. G. Sartakov, and G. Meijer. Spectroscopic characterization of aluminum monofluoride with relevance to laser cooling and trapping. *Phys. Rev. A*, 100:052513, Nov 2019. doi: 10.1103/PhysRevA.100.052513. URL https://link.aps.org/doi/10.1103/PhysRevA.100.052513.

[16] C. Cohen-Tannoudji, B. Diu, and F. Laloë. *Quantenmechanik*. De Gruyter Studium. De Gruyter, 2019. ISBN 9783110639308. URL https://books.google.de/books?id=8jGnDwAAQBAJ.

[17] F.K. Kneubühl and M.W. Sigrist. *Laser*. Teubner Studienbücher Physik. Vieweg+Teubner Verlag, 2015. ISBN 9783322996886. URL https://books.google.de/books?id=8h-EBwAAQBAJ.

[18] O. Svelto. *Principles of Lasers*. Springer US, 2013. ISBN 9781475762662. URL https://books.google.de/books?id=tVLuBwAAQBAJ.

[19] University of Babylon. Optical cavity and laser modes. URL http://www.uobabylon.edu.iq/eprints/publication_2_14877_1775.pdf.

[20] Lasermoden. 2020. URL https://www.ilt.fraunhofer.de/de/studium/laser-tutorial/lasermoden.html.

[21] Katrin Paschke. Hochleistungsdiodenlaser hoher spektraler strahldichte mit geneigtem bragg-gitter als modenfilter. URL https://cuvillier.de/uploads/preview/public_file/2258/9783867277457.pdf.

[22] Johnson J.A. Asplund M.C. and Patterson J.E. The 2018 nobel prize in physics: optical tweezers and chirped pulse amplification. *Anal Bioanal Chem 411*, 1(5001-5005), 2019. doi: https://doi.org/10.1007/s00216-019-01913-z.

[23] A. Weiner. *Ultrafast Optics*. Wiley Series in Pure and Applied Optics. Wiley, 2011. ISBN 9781118211472. URL https://books.google.de/books?id=fhohaV7wJbYC.

[24] Zhiguang Xu, Shulian Zhang, Wenhua Du, Yan Li, Lianqing Zhang, and Jun Zhu. Folded resonator–dual polarization competition laser displacement sensor. *Optics Communications*, 267(1):170–176, 2006. ISSN 0030-4018. doi: https://doi.org/10.1016/j.optcom.2006.06.015. URL https://www.sciencedirect.com/science/article/pii/S0030401806006109.

[25] *User's Manual, Millenia eV.*

[26] Jürgen Eichler, Lothar Dünkel, and Bernd Eppich. Die strahlqualität von lasern – wie bestimmt man beugungsmaßzahl und strahldurchmesser in der praxis? *Laser Technik Journal*, 1(2):63–66, 2004. doi: https://doi.org/10.1002/latj.200790019. URL https://onlinelibrary.wiley.com/doi/abs/10.1002/latj.200790019.

[27] W.R. Bennet A. Javan and D.R. Herriot. The first he-ne-laser: An amplification. *Physics Today*, 1960. doi: https://doi.org/10.1063/1.2811104.

[28] C S Willett. Introduction to gas lasers: population inversion mechanisms. 1 1974. URL https://www.osti.gov/biblio/7156527.

[29] FHI-ELAB. *Manual-Laser-Frequency-Stabilisation.*

[30] Thomas Schneider. *Brillouin Scattering*, pages 269–296. Springer Berlin Heidelberg, Berlin, Heidelberg, 2004. ISBN 978-3-662-08996-5. doi: 10.1007/978-3-662-08996-5_11. URL https://doi.org/10.1007/978-3-662-08996-5_11.

[31] A. Brignon, J.P. Huignard, and John Wiley & Sons. *Phase Conjugate Laser Optics*. Wiley Series in Lasers and Applications. Wiley, 2003. ISBN 9780471439578. URL https://books.google.de/books?id=Uqun_jvJCR8C.

[32] Kireet Semwal and S. C. Bhatt. Study of nd ion as a dopant in yag and glass laser. *International Journal of Physics*, 1(1):15–21, 2013.

[33] J. C. Lehmann. Iodine, a test molecule in modern spectroscopy. *Contemporary Physics*, 19(5):449–467, 1978. doi: 10.1080/00107517808210894. URL https://doi.org/10.1080/00107517808210894.

[34] S. Gerstenkorn, P. Luc, J. Verges, and J. Chevillard. *Atlas du spectre d'absorption de la molécule d'iode*. Number Bd. 1 in Atlas du spectre d'absorption de la molécule d'iode. Laboratoire Aimé Cotton, 1978. URL https://books.google.de/books?id=6-akkgAACAAJ.

[35] S. Gerstenkorn and P. Luc. *Atlas du spectre d'absorption de la molécule d'iode: 14800-20000 cm-1 ; complément: Identification des transitions du système (B-X), assignments of the (B (I2)-X) iodine lines*. Éd. du CNRS, 1986. URL https://books.google.de/books?id=aSnhMgEACAAJ.

[36] High Finesse. *High Finesse WS-8 Wavemeter Datasheet*. URL https://www.highfinesse.com/en/specs.html.

[37] M.H. Havenith. *Infrared Spectroscopy of Molecular Clusters: An Introduction to Intermolecular Forces*. Springer Tracts in Modern Physics. Springer Berlin Heidelberg, 2003. ISBN 9783540454571. URL https://books.google.de/books?id=f7_qCAAAQBAJ.

[38] Nicole Walter. *Spectroscopy Studies on Aluminium Monofluoride*. PhD thesis, 2020, University of Stuttgart.

[39] Monika Wolf. Multi-channel-plates. *Physik in unserer Zeit*, 12(3):90–95, 1981. doi: https://doi.org/10.1002/piuz.19810120305. URL https://onlinelibrary.wiley.com/doi/abs/10.1002/piuz.19810120305.

[40] R.P. Feynman, R.B. Leighton, and M. Sands. *Quantenmechanik*. De Gruyter Studium. De Gruyter, 2015. ISBN 9783110367744. URL https://books.google.de/books?id=z5-nCgAAQBAJ.

[41] G. Herzberg. *Spectra of diatomic molecules*. Molecular spectra and molecular structure. Van Nostrand, 1950. URL https://books.google.de/books?id=rYYotgEACAAJ.

[42] Theresa Julia Zielinski, Erica Harvey, Robert Sweeney, and David M. Hanson. Quantum states of atoms and molecules. *Journal of Chemical Education*, 82 (12):1880, 2005. doi: 10.1021/ed082p1880.2. URL https://doi.org/10.1021/ed082p1880.2.

[43] F.W. Bopp. *Kerne, Hadronen und Elementarteilchen: Eine Einführung*. Teubner Studienbücher Physik. Vieweg+Teubner Verlag, 1989. ISBN 9783519030683. URL https://books.google.de/books?id=BDsrAQAACAAJ.

[44] Robert C. Dunbar. Deriving the maxwell distribution. *Journal of Chemical Education*, 59(1):22, 1982. doi: 10.1021/ed059p22. URL https://doi.org/10.1021/ed059p22.

[45] A.E. Siegman. *Lasers*. University Science Books, 1986. ISBN 9780935702118. URL https://books.google.de/books?id=1BZVwUZLTkAC.

[46] A.M. Kelley. *Condensed-Phase Molecular Spectroscopy and Photophysics*. Wiley, 2012. ISBN 9781118493069. URL https://books.google.de/books?id=fC3eq9IJaN8C.

[47] J.J. Olivero and R.L. Longbothum. Empirical fits to the voigt line width: A brief review. *Journal of Quantitative Spectroscopy and Radiative Transfer*, 17(2):233–236, 1977. ISSN 0022-4073. doi: https://doi.org/10.1016/0022-4073(77)90161-3. URL https://www.sciencedirect.com/science/article/pii/0022407377901613.

[48] T. Arndt. *Lambert-Beer-Gesetz*, pages 1432–1433. Springer Berlin Heidelberg, Berlin, Heidelberg, 2019. ISBN 978-3-662-48986-4. doi: 10.1007/978-3-662-48986-4_1822. URL https://doi.org/10.1007/978-3-662-48986-4_1822.

[49] G. Meijer, W.M.G. Ubachs, J.J. ter Meulen, and A. Dymanus. High resolution lamb-dip spectroscopy on od and sicl in a molecular beam. *Chemical Physics Letters*, 139:603, 1987. ISSN 0009-2614. doi: 10.1016/0009-2614(87)87350-5.

[50] William R. Bennett Jr. history of hole burning. *Phys. Today*, 61, 2008. doi: 10.1063/1.2930750. URL https://physicstoday.scitation.org/doi/10.1063/1.2930750.

[51] Maximilian Doppelbauer, Nicole Walter, Simon Hofsäss, Silvio Marx, Hanns Schewe, Sebastian Kray, Jesús Pérez-Ríos, Boris Sartakov, Stefan Truppe, and Gerard Meijer. Characterisation of the $b^3\sigma^+, v = 0$ state and its interaction with the $a^1\pi$ state in aluminium monofluoride. 08 2020.

[52] *private communication in mails with Sirah Lasertechnik.*

[53] Nicole Walter, Seifert Johannes, Silvio Marx, Boris Sartakov, Stefan Truppe, and Gerard Meijer. Spectroscopic characterisation of the lowest triplet state and of singlet-triplet "doorway" levels of aluminum monofluoride. in press.